

Comparison of transverse single-spin asymmetries for forward π^0 production in polarized pp , pAl and pAu collisions at nucleon pair c.m. energy $\sqrt{s_{NN}} = 200$ GeV

J. Adam⁶, L. Adamczyk², J. R. Adams³⁹, J. K. Adkins³⁰, G. Agakishiev²⁸, M. M. Aggarwal⁴¹, Z. Ahammed⁶¹, I. Alekseev^{3,35}, D. M. Anderson⁵⁵, A. Aparin²⁸, E. C. Aschenauer⁶, M. U. Ashraf¹¹, F. G. Atetalla²⁹, A. Attri⁴¹, G. S. Averichev²⁸, V. Bairathi⁵³, K. Barish¹⁰, A. Behera⁵², R. Bellwied²⁰, A. Bhasin²⁷, J. Bielcik¹⁴, J. Bielcikova³⁸, L. C. Bland⁶, I. G. Bordyuzhin³, J. D. Brandenburg⁶, A. V. Brandin³⁵, H. Caines⁶⁴, M. Calderón de la Barca Sánchez⁸, D. Cebra⁸, I. Chakaberia^{29,6}, P. Chaloupka¹⁴, B. K. Chan⁹, Z. Chang⁶, N. Chankova-Bunzarova²⁸, A. Chatterjee¹¹, D. Chen¹⁰, J. H. Chen¹⁸, X. Chen⁴⁸, Z. Chen⁴⁹, J. Cheng⁵⁷, M. Cherney¹³, M. Chevalier¹⁰, S. Choudhury¹⁸, W. Christie⁶, X. Chu⁶, H. J. Crawford⁷, M. Csanád¹⁶, M. Daugherty¹, T. G. Dedovich²⁸, I. M. Deppner¹⁹, A. A. Derevschikov⁴³, L. Didenko⁶, X. Dong³¹, J. L. Drachenberg¹, J. C. Dunlop⁶, N. Elsey⁶³, J. Engelage⁷, G. Eppley⁴⁵, S. Esumi⁵⁸, O. Evdokimov¹², A. Ewigleben³², O. Eyser⁶, R. Fatemi³⁰, S. Fazio⁶, P. Federic³⁸, J. Fedorisin²⁸, C. J. Feng³⁷, Y. Feng⁴⁴, P. Filip²⁸, E. Finch⁵¹, Y. Fisyak⁶, A. Francisco⁶⁴, L. Fulek², C. A. Gagliardi⁵⁵, T. Galatyuk¹⁵, F. Geurts⁴⁵, A. Gibson⁶⁰, K. Gopal²³, D. Grosnick⁶⁰, W. Gryn⁶, A. I. Hamad²⁹, A. Hamed⁵, S. Harabasz¹⁵, J. W. Harris⁶⁴, S. He¹¹, W. He¹⁸, X. H. He²⁶, S. Heppelmann⁸, S. Heppelmann⁴², N. Herrmann¹⁹, E. Hoffman²⁰, L. Holub¹⁴, Y. Hu¹⁸, H. Z. Huang⁹, S. L. Huang⁵², T. Huang³⁷, X. Huang⁵⁷, T. J. Humanic³⁹, G. Igo⁹, D. Isenhowe¹, W. W. Jacobs²⁵, C. Jena²³, A. Jentsch⁶, Y. Ji⁴⁸, J. Jia^{6,52}, K. Jiang⁴⁸, X. Ju⁴⁸, E. G. Judd⁷, S. Kabana⁵³, M. L. Kabir¹⁰, S. Kagamaster³², D. Kalinkin²⁵, K. Kang⁵⁷, D. Kapukchyan¹⁰, K. Kauder⁶, H. W. Ke⁶, D. Keane²⁹, A. Kechechyan²⁸, M. Kelsey³¹, Y. V. Khyzhniak³⁵, D. P. Kikola⁶², C. Kim¹⁰, B. Kimelman⁸, D. Kincses¹⁶, I. Kisel¹⁷, A. Kiselev⁶, L. Kochenda³⁵, L. K. Kosarzewski¹⁴, L. Kramarik¹⁴, P. Kravtsov³⁵, K. Krueger⁴, L. Kumar⁴¹, S. Kumar²⁶, R. Kunnawalkam Elayavalli⁶³, J. H. Kwasizur²⁵, R. Lacey⁵², S. Lan¹¹, J. M. Landgraf⁶, J. Lauret⁶, A. Lebedev⁶, R. Lednický²⁸, J. H. Lee⁶, Y. H. Leung³¹, C. Li⁴⁸, W. Li⁴⁵, W. Li⁵⁰, X. Li⁴⁸, Y. Li⁵⁷, Y. Liang²⁹, R. Lichenik³⁸, T. Lin⁵⁵, Y. Lin¹¹, M. A. Lisa³⁹, F. Liu¹¹, H. Liu²⁵, P. Liu⁵², P. Liu⁵⁰, T. Liu⁶⁴, X. Liu³⁹, Y. Liu⁵⁵, Z. Liu⁴⁸, T. Ljubicic⁶, W. J. Llope⁶³, R. S. Longacre⁶, N. S. Lukow⁵⁴, X. Luo¹¹, G. L. Ma⁵⁰, L. Ma¹⁸, R. Ma⁶, Y. G. Ma⁵⁰, N. Magdy¹², R. Majka⁶⁴, D. Mallick³⁶, S. Margetis²⁹, C. Markert⁵⁶, H. S. Matis³¹, J. A. Mazer⁴⁶, N. G. Minaev⁴³, S. Mioduszewski⁵⁵, B. Mohanty³⁶, I. Mooney⁶³, D. A. Morozov⁴³, M. Nagy¹⁶, J. D. Nam⁵⁴, Md. Nasim²², K. Nayak¹¹, D. Neff⁹, J. M. Nelson⁷, D. B. Nemes⁶⁴, M. Nie⁴⁹, G. Nigmatkulov³⁵, T. Niida⁵⁸, L. V. Nogach⁴³, T. Nonaka⁵⁸, A. S. Nunes⁶, G. Odyniec³¹, A. Ogawa⁶, S. Oh³¹, V. A. Okorokov³⁵, B. S. Page⁶, R. Pak⁶, A. Pandav³⁶, Y. Panebratsev²⁸, B. Pawlik⁴⁰, D. Pawlowska⁶², H. Pei¹¹, C. Perkins⁷, L. Pinsky²⁰, R. L. Pinter¹⁶, J. Pluta⁶², J. Porter³¹, M. Posik⁵⁴, N. K. Pruthi⁴¹, M. Przybycien², J. Putschke⁶³, H. Qiu²⁶, A. Quintero⁵⁴, S. K. Radhakrishnan²⁹, R. L. Ray⁵⁶, R. Reed³², H. G. Ritter³¹, O. V. Rogachevskiy²⁸, J. L. Romero⁸, L. Ruan⁶, J. Rusnak³⁸, N. R. Sahoo⁴⁹, H. Sako⁵⁸, S. Salur⁴⁶, J. Sandweiss⁶⁴, S. Sato⁵⁸, W. B. Schmidke⁶, N. Schmitz³³, B. R. Schweid⁵², F. Seck¹⁵, J. Seger¹³, M. Sergeeva⁹, R. Seto¹⁰, P. Seyboth³³, N. Shah²⁴, E. Shahaliev²⁸, P. V. Shanmuganathan⁶, M. Shao⁴⁸, A. I. Sheikh²⁹, W. Q. Shen⁵⁰, S. S. Shi¹¹, Q. Y. Shou⁵⁰, E. P. Sichtermann³¹, R. Sikora², M. Simko³⁸, J. Singh⁴¹, S. Singha²⁶, N. Smirnov⁶⁴, W. Solyst²⁵, P. Sorensen⁶, H. M. Spinka⁴, B. Srivastava⁴⁴, T. D. S. Stanislaus⁶⁰, M. Stefaniak⁶², D. J. Stewart⁶⁴, M. Strikhanov³⁵, B. Stringfellow⁴⁴, A. A. P. Suaide⁴⁷, M. Sumera³⁸, B. Summa⁴², X. M. Sun¹¹, X. Sun¹², Y. Sun⁴⁸, Y. Sun²¹, B. Surrow⁵⁴, D. N. Svirida³, P. Szymanski⁶², A. H. Tang⁶, Z. Tang⁴⁸, A. Taranenko³⁵, T. Tarnowsky³⁴, J. H. Thomas³¹, A. R. Timmins²⁰, D. Tlusty¹³, M. Tokarev²⁸, C. A. Tomkiel³², S. Trentalange⁹, R. E. Tribble⁵⁵, P. Tribedy⁶, S. K. Tripathy¹⁶, O. D. Tsai⁹, Z. Tu⁶, T. Ullrich⁶, D. G. Underwood⁴, I. Upsal^{49,6}, G. Van Buren⁶, J. Vanek³⁸, A. N. Vasiliev⁴³, I. Vassiliev¹⁷, F. Videbæk⁶, S. Vokal²⁸, S. A. Voloshin⁶³, F. Wang⁴⁴, G. Wang⁹, J. S. Wang²¹, P. Wang⁴⁸, Y. Wang¹¹, Y. Wang⁵⁷, Z. Wang⁴⁹, J. C. Webb⁶, P. C. Weidenkaff¹⁹, G. D. Westfall³⁴, H. Wieman³¹, S. W. Wissink²⁵, R. Witt⁵⁹, Y. Wu¹⁰, Z. G. Xiao⁵⁷, G. Xie³¹, W. Xie⁴⁴, H. Xu²¹, N. Xu³¹, Q. H. Xu⁴⁹, Y. F. Xu⁵⁰, Y. Xu⁴⁹, Z. Xu⁶, Z. Xu⁹, C. Yang⁴⁹, Q. Yang⁴⁹, S. Yang⁶, Y. Yang³⁷, Z. Yang¹¹, Z. Ye⁴⁵, Z. Ye¹², L. Yi⁴⁹, K. Yip⁶, H. Zbroszczyk⁶², W. Zha⁴⁸, C. Zhang⁵², D. Zhang¹¹, S. Zhang⁴⁸, S. Zhang⁵⁰, X. P. Zhang⁵⁷, Y. Zhang⁴⁸, Y. Zhang¹¹, Z. J. Zhang³⁷, Z. Zhang⁶, Z. Zhang¹², J. Zhao⁴⁴, C. Zhong⁵⁰, C. Zhou⁵⁰, X. Zhu⁵⁷, Z. Zhu⁴⁹, M. Zurek³¹, M. Zyzak¹⁷

¹Abilene Christian University, Abilene, Texas 79699

²AGH University of Science and Technology, FPACS, Cracow 30-059, Poland

³Alikhanov Institute for Theoretical and Experimental Physics NRC "Kurchatov Institute", Moscow 117218, Russia

⁴Argonne National Laboratory, Argonne, Illinois 60439

⁵American University of Cairo, New Cairo 11835, New Cairo, Egypt

⁶Brookhaven National Laboratory, Upton, New York 11973

⁷University of California, Berkeley, California 94720

- ⁸University of California, Davis, California 95616
- ⁹University of California, Los Angeles, California 90095
- ¹⁰University of California, Riverside, California 92521
- ¹¹Central China Normal University, Wuhan, Hubei 430079
- ¹²University of Illinois at Chicago, Chicago, Illinois 60607
- ¹³Creighton University, Omaha, Nebraska 68178
- ¹⁴Czech Technical University in Prague, FNSPE, Prague 115 19, Czech Republic
- ¹⁵Technische Universität Darmstadt, Darmstadt 64289, Germany
- ¹⁶ELTE Eötvös Loránd University, Budapest, Hungary H-1117
- ¹⁷Frankfurt Institute for Advanced Studies FIAS, Frankfurt 60438, Germany
- ¹⁸Fudan University, Shanghai, 200433
- ¹⁹University of Heidelberg, Heidelberg 69120, Germany
- ²⁰University of Houston, Houston, Texas 77204
- ²¹Huzhou University, Huzhou, Zhejiang 313000
- ²²Indian Institute of Science Education and Research (IISER), Berhampur 760010, India
- ²³Indian Institute of Science Education and Research (IISER) Tirupati, Tirupati 517507, India
- ²⁴Indian Institute Technology, Patna, Bihar 801106, India
- ²⁵Indiana University, Bloomington, Indiana 47408
- ²⁶Institute of Modern Physics, Chinese Academy of Sciences, Lanzhou, Gansu 730000
- ²⁷University of Jammu, Jammu 180001, India
- ²⁸Joint Institute for Nuclear Research, Dubna 141 980, Russia
- ²⁹Kent State University, Kent, Ohio 44242
- ³⁰University of Kentucky, Lexington, Kentucky 40506-0055
- ³¹Lawrence Berkeley National Laboratory, Berkeley, California 94720
- ³²Lehigh University, Bethlehem, Pennsylvania 18015
- ³³Max-Planck-Institut für Physik, Munich 80805, Germany
- ³⁴Michigan State University, East Lansing, Michigan 48824
- ³⁵National Research Nuclear University MEPhI, Moscow 115409, Russia
- ³⁶National Institute of Science Education and Research, HBNI, Jatni 752050, India
- ³⁷National Cheng Kung University, Tainan 70101
- ³⁸Nuclear Physics Institute of the CAS, Rez 250 68, Czech Republic
- ³⁹Ohio State University, Columbus, Ohio 43210
- ⁴⁰Institute of Nuclear Physics PAN, Cracow 31-342, Poland
- ⁴¹Panjab University, Chandigarh 160014, India
- ⁴²Pennsylvania State University, University Park, Pennsylvania 16802
- ⁴³NRC "Kurchatov Institute", Institute of High Energy Physics, Protvino 142281, Russia
- ⁴⁴Purdue University, West Lafayette, Indiana 47907
- ⁴⁵Rice University, Houston, Texas 77251
- ⁴⁶Rutgers University, Piscataway, New Jersey 08854
- ⁴⁷Universidade de São Paulo, São Paulo, Brazil 05314-970
- ⁴⁸University of Science and Technology of China, Hefei, Anhui 230026
- ⁴⁹Shandong University, Qingdao, Shandong 266237
- ⁵⁰Shanghai Institute of Applied Physics, Chinese Academy of Sciences, Shanghai 201800
- ⁵¹Southern Connecticut State University, New Haven, Connecticut 06515
- ⁵²State University of New York, Stony Brook, New York 11794
- ⁵³Instituto de Alta Investigación, Universidad de Tarapacá, Arica 1000000, Chile
- ⁵⁴Temple University, Philadelphia, Pennsylvania 19122
- ⁵⁵Texas A&M University, College Station, Texas 77843
- ⁵⁶University of Texas, Austin, Texas 78712
- ⁵⁷Tsinghua University, Beijing 100084
- ⁵⁸University of Tsukuba, Tsukuba, Ibaraki 305-8571, Japan
- ⁵⁹United States Naval Academy, Annapolis, Maryland 21402
- ⁶⁰Valparaiso University, Valparaiso, Indiana 46383
- ⁶¹Variable Energy Cyclotron Centre, Kolkata 700064, India
- ⁶²Warsaw University of Technology, Warsaw 00-661, Poland
- ⁶³Wayne State University, Detroit, Michigan 48201 and
- ⁶⁴Yale University, New Haven, Connecticut 06520

(STAR Collaboration)

The STAR Collaboration reports a measurement of the transverse single-spin asymmetries, A_N , for neutral pions produced in polarized proton collisions with protons (pp), with aluminum nuclei (pAl) and with gold nuclei (pAu) at a nucleon-nucleon center-of-mass energy of 200 GeV. Neutral pions are observed in the forward direction relative to the transversely polarized proton beam, in

the pseudo-rapidity region $2.7 < \eta < 3.8$. Results are presented for π^0 s observed in the STAR FMS electromagnetic calorimeter in narrow Feynman x (x_F) and transverse momentum (p_T) bins, spanning the range $0.17 < x_F < 0.81$ and $1.7 < p_T < 6.0$ GeV/c. For fixed $x_F < 0.47$, the asymmetries are found to rise with increasing transverse momentum. For larger x_F , the asymmetry flattens or falls as p_T increases. Parametrizing the ratio $r(A) \equiv A_N(pA)/A_N(pp) = A^P$ over the kinematic range, the ratio $r(A)$ is found to depend only weakly on A , with $\langle P \rangle = -0.027 \pm 0.005$. No significant difference in P is observed between the low- p_T region, $p_T < 2.5$ GeV/c, where gluon saturation effects may play a role, and the high- p_T region, $p_T > 2.5$ GeV/c. It is further observed that the value of A_N is significantly larger for events with a large- p_T isolated π^0 than for events with a non-isolated π^0 accompanied by additional jet-like fragments. The nuclear dependence $r(A)$ is similar for isolated and non-isolated π^0 events.

I. INTRODUCTION

The measurements and the evolving interpretations of transverse single-spin asymmetries for forward pion production in high energy pp collisions have a rich history [1–7]. These measurements guided the development of Quantum Chromo-Dynamics (QCD) based models that incorporated quark helicity conservation, QCD factorization, the nature of initial state parton motion or angular momentum, and the dynamics of fragmentation within the scattering processes for polarized protons. The new transverse asymmetry measurements, presented here, again challenge aspects of current models for the application of QCD to the spin dependence of cross sections. The π^0 single-spin asymmetry, A_N , is measured as a function of pion kinematics for collisions between polarized protons and protons (pp), aluminum nuclei (pAl) and gold nuclei (pAu). Because A_N for this process is expected to be very sensitive to the QCD fields in the vicinity of a struck quark, the nuclear dependence of A_N should be sensitive to phenomena that modify the local fields, for example, gluon saturation effects.

This analysis presents the dependence of A_N in the forward π^0 production process, $p^\uparrow + p(\text{or } A) \rightarrow \pi^0 + X$. It is useful to first define a simple azimuthal angle-dependent asymmetry, $a_N(x_F, p_T, \phi)$, as the ratio of the difference in cross section for the two proton transverse spin states, σ^\uparrow and σ^\downarrow , to the sum of those cross sections for a pion produced at x_F (Feynman X) and p_T (transverse momentum),

$$a_N(x_F, p_T, \phi) = \frac{\sigma^\uparrow(x_F, p_T, \phi) - \sigma^\downarrow(x_F, p_T, \phi)}{\sigma^\uparrow(x_F, p_T, \phi) + \sigma^\downarrow(x_F, p_T, \phi)} \quad (1)$$

$$= A_N(x_F, p_T) \cos \phi. \quad (2)$$

The three components of pion momentum are specified with coordinates x_F , p_T and ϕ . The dependence of the pion differential cross section on transverse spin, expressed as the pion momentum dependent asymmetry $a_N(x_F, p_T, \phi)$ and the transverse single-spin asymmetry, $A_N(x_F, p_T)$, are defined in terms of the simple asymmetry accordingly, (Eq. 2). Referring to a right-handed coordinate system, an initial state polarized proton is referred to as spin “up” if it has a positive spin projection along the y axis while proton momentum is along the z axis. This polarized proton collides with an unpolarized proton or nucleus traveling along the $-z$ axis. A forward

pion has a positive longitudinal component of momentum p_L^π , given by a positive fraction $x_F = 2\frac{p_L^\pi}{\sqrt{s}}$ of the polarized proton momentum. The angle ϕ is the pion azimuthal angle about the z axis measured from the x axis positive direction. Equation 2 defines $A_N(x_F, p_T)$ in terms of cross sections, which are differential in x_F , p_T and ϕ , with superscript arrows indicating the spin directions up or down, respectively. Symmetry requires that the ϕ dependence be proportional to $\cos \phi$.

II. THE RELATION BETWEEN SCATTERING WITH LONGITUDINAL AND TRANSVERSE POLARIZATION

The unique features of the spin dependence of scattering from quarks or gluons in transversely polarized protons are best understood when contrasted with scattering of partons in longitudinally (helicity) polarized protons. For a longitudinally polarized Dirac fermion, the dependence of cross section on the initial state spin is connected to helicity conservation. For a relativistic electron or quark, the absorption or emission of a virtual photon (or similarly a gluon) cannot flip the helicity of a relativistic fermion. However, in a one dimensional scattering example, where a virtual photon is in a particular helicity state, and is absorbed by a free quark at rest, the longitudinal spin component of the quark must flip as one unit of photon spin is absorbed by the quark, changing the struck quark spin by one unit. Such a photon can be absorbed by only one of the two possible initial quark spin states, so cross sections thus can depend on initial state quark spin component along the final state direction or on the final state helicity. But with absorption from a transversely polarized quark, where transverse spin states are composed of equal magnitude combinations of the two helicity states, the cross section is the same for either transverse spin state. For scattering between small mass electrons and quarks, this generalizes to a cross section, that depends on Dirac fermion helicities but not on their transverse spins. Any cross section dependence on transverse spin is associated with the negligibly small helicity flip amplitudes.

In the original quark model, where the spin of a polarized proton was attributed to the polarized quarks, it was clear that the longitudinal polarization of these quarks

could be observed by the double helicity measurements in scattering between protons and electrons. Because deep inelastic scattering cross sections were most sensitive to the up quarks, due to their larger electric charge, it was a very early prediction of the quark model that the longitudinal polarization of up quarks within the polarized proton could be observed by measuring the dependence of the lepton-proton cross section on the proton and lepton longitudinal spins [8].

The longitudinal double spin lepton-proton scattering measurements provided the mechanism for the first measurements of quark momentum dependent longitudinally polarized quark distributions in a longitudinally polarized proton [9, 10]. Similar longitudinal double spin proton-proton cross sections depended upon the longitudinal polarization of partons, including gluons. Measurements and analysis of longitudinally polarized protons remain an important topic for the STAR experiment, to constrain longitudinal polarization densities of partons in the proton. Global analyses of many experiments [11–13] have integrated the experimental results.

In a frame where the proton was highly relativistic, where each quark momentum was nearly parallel to the proton momentum, the cross section did depend directly on the helicity of the struck quark. The cross section associated with a longitudinally polarized, nearly free, quark was calculable from hard scattering in helicity conserving perturbative processes. The longitudinal double spin asymmetry was then sensitive to the longitudinally polarized struck quark in the longitudinally polarized proton. However, the scattering cross section for such a quark did not depend on the components of its spin measured along a transverse axis. Such a dependence would have been associated with the parton flipping helicity as it interacted, by absorbing or emitting a photon or gluon. Because the quark helicity-flip amplitude was vanishingly small at high energies, early predictions, that the transverse spin dependence of the quark scattering process should vanish at high energy, implied that A_N should be small for high energy collisions [14]. Transverse spin dependence of cross sections are known to be further suppressed because such dependencies required an interference between helicity amplitudes with different phases. Such a phase-shifted amplitude is not present in the hard scattering part of leading twist perturbative QCD (pQCD) processes.

From the above discussion, it is seen that the helicity conserving amplitudes, which apparently dominate the calculation of unpolarized cross sections or longitudinal polarization dependence of these cross sections, do not significantly contribute to the large transverse spin asymmetries A_N that have been observed in pp collisions.

III. MECHANISMS FOR NON-ZERO TRANSVERSE ASYMMETRY

The measurement of transverse spin asymmetries is sensitive to effects that are very different than the physics responsible for longitudinal asymmetries. The traditional pQCD calculations for hard scattering from protons relied on collinear factorization [15], where all parton momenta were characterized as propagating parallel to the parent proton momentum. Within this framework, the transverse spin dependence was limited by the suppression of hard scattering helicity-flip amplitudes. But more nuanced pictures of scattering of quarks in a transversely polarized proton have emerged, utilizing parton density distributions that characterize both transverse and longitudinal components of parton momentum. With such a parton density distribution, the initial state parton motion need not be parallel to the proton momentum, meaning that a helicity frame for the proton may not completely align with the helicity frame of the quark.

A transverse momentum offset of \vec{k}_T , representing the average transverse momentum of the initial/final state quark relative to the initial/final state parent hadron, respectively, is added to the transverse momentum \vec{P}_T from the hard scattering process to form the observed pion transverse momentum, $p_T^\pi = |\vec{P}_T + \vec{k}_T|$. So while the quark scattering cross section has little direct dependence on the transverse spin of the quark, the pion production cross section can depend on the transverse spin of the proton through initial and final state interactions leading to non-zero \vec{k}_T . If this bias of \vec{k}_T is correlated with the transverse spin of the proton, then non-zero A_N will result. This kind of proton spin dependence of the observed pion cross section is amplified by the extreme p_T dependence of the hard pion cross section.

The general expectation that the pion A_N should fall with increasing p_T for p_T above a nominal QCD momentum scale can be demonstrated in a simple model. If one assumes that the forward hard scattering cross section of a quark, with momentum fraction x , falls with increasing transverse momentum, p_T , by a power law form with power N , then

$$\frac{d\sigma}{dp_T} \propto p_T^{-N}, \quad (3)$$

where $p_T = |\vec{P}_T|$. If the scattered quark acquires transverse momentum $\vec{k}_T = \pm k_T \hat{x}$ from initial or final state interactions that is correlated with the polarized proton spin in the $\pm \hat{y}$ directions, then we see that A_N will also fall with increasing p_T . Assuming the hard scattering transverse momentum is much greater than the initial state or final state transverse momentum ($p_T \gg k_T$), then the difference in cross section when p_T^π is measured along the $\pm \hat{x}$ direction leads to A_N as in Eq. 4. If we assume a cross section form for p_T , as in Eq. 3, expressing

A_N as a left-right asymmetry, we have

$$\begin{aligned}
 A_N(x_F, p_T) &= \frac{\sigma^\uparrow(x_F, p_T, 0) - \sigma^\uparrow(x_F, p_T, \pi)}{\sigma^\uparrow(x_F, p_T, 0) + \sigma^\uparrow(x_F, p_T, \pi)} \\
 &\simeq \frac{(p_T^\pi - k_T)^{-N} - (p_T^\pi + k_T)^{-N}}{(p_T^\pi - k_T)^{-N} + (p_T^\pi + k_T)^{-N}} \quad (4) \\
 &\simeq N \frac{k_T}{p_T^\pi}
 \end{aligned}$$

for small k_T/p_T^π . This demonstrates that if the k_T shift is independent of the hard scattering p_T , it is very natural to expect the magnitude of the asymmetry to fall with increasing observed transverse momentum p_T at large p_T . In previous measurements [5] of the p_T dependence for A_N with charged pions, the asymmetry has been seen to increase with p_T up to about $p_T < 1$ GeV/c. In an earlier STAR measurement [7], it was observed that there was little evidence for A_N falling with p_T up to at least 3 GeV/c. In this paper, the data are analyzed to separate the independent effects of p_T and x_F .

Two classes of models have been introduced for forward A_N , both involved the hard scattering of a leading momentum quark in the polarized proton and both depended upon secondary interactions to generate a spin dependent contribution \vec{k}_T to the pion final state transverse momentum. The Siverson effect [16] involved an initial state interaction before the hard scattering of a quark in a polarized proton, leading to initial state parton transverse momentum that depended on the proton transverse polarization. The Collins effect [17] generated a transverse spin dependent component to the final state pion transverse momentum from the fragmentation process of the scattered quark, which retained its initial state transverse polarization through the hard scattering process. Closely related to Collins and Siverson models was an approach involving higher twist calculation, where the scattered quark was correlated with a soft gluon, which also lead to a significant transverse asymmetry [18].

Many model calculations attempt to describe forward pion transverse spin asymmetries using one of these approaches. While for both types of models the basic mechanism involves the production of a final state pion from fragmentation of a hard scattered parton, only the Collins approach explains large A_N arising from the fragmentation process. In contrast to pion production, jet production does not involve fragmentation. The Collins effect therefore does not contribute to that asymmetry. Jet A_N measurements in this kinematic region have been published and the values of A_N were observed to be smaller than measured pion asymmetries [19].

Both the Siverson and the Collins approaches introduced a parton transverse momentum relative to the initial or final state hadron momentum to generate a transverse asymmetry without violating helicity conservation. In the Siverson picture, transverse momentum of initial state quarks can be connected to the initial state orbital angular momentum of a struck quark along the polarization axis. While an orbiting quark does not, on average,

have transverse momentum, Siverson argued that absorptive effects could break the left-right symmetric parton k_T distribution to generate the required non-vanishing average $k_T = \langle \vec{k}_T \cdot \hat{x} \rangle$. Even though absorption does introduce phase changes, the calculation of this phase in the conventional perturbative calculation was not fully appreciated until it was noted in [20] that the Wilson line contribution, formally required in the pQCD calculation, did provide exactly the needed phase change for a non-zero A_N [21].

The emerging physical picture is that unlike the case for longitudinal spin dependence, the observed large values of A_N derive not from the spin dependence of the hard scattering process between the pair of partons, but from the interaction between the scattered quark and the other constituents or fragments of the polarized proton. While from symmetry, A_N must vanish at $p_T = 0$, the example of Eq. 4 demonstrates that the asymmetry is expected to fall with transverse momentum above some nominal scale, \vec{k}_T . There have been many calculations in recent years based on Collins, Siverson or Twist-3 collinear methods with a goal to reproduce the basic nature of A_N dependence on kinematics [22–26]. A general feature of these calculations was that they could reproduce the dependence of A_N on x_F , but like the simple description from Eq. 4, A_N was generally predicted to fall with p_T in the p_T range of this measurement.

IV. MEASUREMENTS OF A_N IN PROTON-NUCLEUS COLLISIONS

If the observed transverse single-spin dependent amplitude for forward pion production arises completely from the localized quark-gluon hard scattering process, then the environment that provides the soft gluon in the second proton or nucleus would not likely impact A_N . But we know that the important source of A_N is not the hard quark-gluon scattering process itself but primarily involves the additional interactions with other fields in the nucleon or nucleus, perhaps manifested by the generation of parton transverse momentum relative to the parent hadron momentum. Because the mechanism responsible for transverse spin asymmetries is not a simple local leading twist interaction but depends on the environment in which a parton interaction occurs, it is clear that A_N could be different for pp , pAl and pAu collisions. Even the simple model of Eq. 4 reminds us that a change in the shape of the p_T dependence for pion production due to either nuclear absorption, rescattering, or modification of the gluon distribution, could lead to dependence of A_N on nuclear size.

The measurement of how A_N changes when the beam remnant partons of the proton are replaced with spectator partons of a nucleus is a subject of this paper. It is clear that the phase from the Wilson line integral, a line integral of the gauge vector potential color field along

the struck quark trajectory, can give rise to color forces between the struck quark and the rest of the polarized proton. If there are also important color forces between the hard scattering constituents and the residual spectator nucleus, then nuclear dependence of A_N in pA scattering could result. Studies of the spin dependence of the interaction between the interacting quark and the residual spectator nucleus have predicted large nuclear A -dependent transverse spin effects but at a lower transverse momentum scale than that of this analysis [27]. A more recent calculation was based on lensing forces, with specific reference to the kinematics of this experiment [28]. The model addressed the dependence of A_N on nuclear saturation as well as the p_T dependence of A_N .

One mechanism that could provide nuclear A dependence of A_N relates to the increase in gluon density in the soft gluon distribution probed in forward scattering. It is predicted that at low gluon x , when the gluon density becomes large, saturation effects begin to play an important role. For interactions between soft gluons and hard partons producing scattered pions in the range $1.5 < p_T < 2.5$ GeV/ c , saturation effects might modify the interaction, creating significant differences between the corresponding scattering process in pp and pA collisions. Specific saturation models, such as the Color Glass Condensate [29], predict interactions of the scattered quark with a condensate of gluons rather than a hard scatter from a single gluon. Such saturation calculations predict a change in the p_T distribution of the cross section in regions of p_T near the saturation scale, with a suppression of the cross section that increases with nuclear size. In the $p_T \approx 2$ GeV/ c range and at more forward pseudo-rapidity than this measurement ($\eta \approx 4$), STAR has reported that the nuclear modification ratio R_{dAu} in dAu scattering to produce π^0 mesons [30] is significantly less than unity, suggesting a difference in the scattering process as the size of the nucleus is varied. In the same p_T and rapidity range presented here, measurements of the nuclear modification factors for charged hadrons (mostly charged pions) [31] showed suppression in R_{dAu} . This paper addresses the nuclear dependence of A_N , noting, in particular, the lower end of the p_T range where evidence for saturation effects has already been seen in the corresponding dA cross sections [30].

V. PHOTON AND π^0 DETECTION IN THE FMS

These data from the Solenoidal Tracker At RHIC (STAR) experiment at the Relativistic Heavy Ion Collider (RHIC) were collected during the 2015 RHIC run, involving collisions between nucleons at center-of-mass energy $\sqrt{s_{NN}} = 200$ GeV per nucleon pair. The photon pair from the decay of the π^0 was detected with the STAR forward electromagnetic calorimeter, referred to as the Forward Meson Spectrometer (FMS) [32]. To measure A_N for forward π^0 production, the STAR detectors

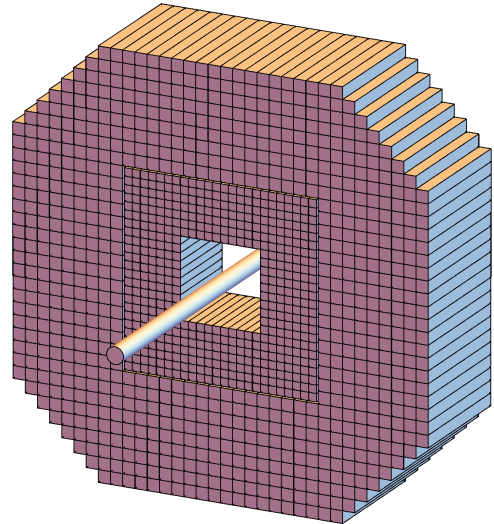


FIG. 1. The layout for the FMS calorimeter around the RHIC beam-line located about seven meters west of the nominal STAR interaction point. The FMS consists of lead glass blocks with lengths corresponding to 18 radiation lengths. There are 788 outer blocks with front face dimensions of 5.8×5.8 cm. and 476 inner blocks with front face dimensions of 3.8×3.8 cm.

used in this analysis were the FMS and the Beam-Beam Counters (BBC).

The two RHIC beams (yellow and blue beams) are bunched with up to 120 bunches in each ring. The small angle scattering from the blue beam is associated with positive rapidity. Only 111 bunches in each beam are filled and a contiguous set of 9 bunches (the abort gap) are unfilled. Bunch spacing is 106 ns and the transverse polarization pattern is chosen for each fill according to a predefined pattern (either alternating the polarization direction from bunch to bunch or for pairs of bunches). The blue beam polarization ranged between 50% and 60%.

The BBCs are located at a distance of ± 3.75 meters east and west of the nominal STAR interaction point, concentric with the beam line, and covering pseudo-rapidity range $3.3 < \eta < 5.2$ [33, 34]. On both the east and west sides of STAR, each BBC detector consists of an inner and outer hexagonal plane of scintillators. For heavy-ion collisions, the summed energy deposited in the BBC detectors is related to charged particle multiplicity in nucleus-nucleus collisions and is sensitive to the event collision centrality. As discussed below, for pA collisions we remove events with small signals in the east BBC, on the opposite side to the FMS, to reduce single beam background.

The FMS is a Pb-glass electromagnetic calorimeter consisting of 1264 rectangular lead glass blocks or cells,

stacked in a wall with front surface transverse to the STAR beam line as shown in Fig. 1. The FMS covers the range of forward pseudo-rapidity, $2.7 < \eta < 3.8$. The blocks are of two types, small and large cells. Details about the detection of π^0 s in the STAR FMS have been discussed elsewhere [32].

The small and large FMS cells have Pb-glass with different compositions. For small and large cells the ratio of cell sizes is chosen to be proportional to the ratio of Molière radii (transverse electro-magnetic shower dimension); therefore a photon in the large cells will deposit its energy into a similar number of cells as a photon of the same energy in the small cells. For a 10 GeV photon, the shower distributes measurable energy into about 10 cells. For higher energy photons, the number of involved cells increases. For a 30 GeV photon from the nominal interaction point, incident at the center of a cell, about 80% of the photon energy is deposited in that cell. Fitting the distribution of energy in cells to an expected distribution from a known shower shape, the transverse coordinates of the incident photon (at shower maximum depth) can be obtained with a resolution of about 20% of the cell dimension.

In the kinematic range discussed in this paper, observed photons from π^0 decays have a separation ranging from a few cells to less than one cell. For the highest energy π^0 s, above 60 GeV, the shower shape from the two photons starts to overlap into a small cell single cluster. Therefore, to reconstruct the highest energy π^0 s, the distribution of deposited energies in cells is fitted to a two photon hypothesis, with parameters that represent the two photon energies and transverse position coordinates. The quality of these fits begins to degrade when the photon separation is on the order of a single cell width.

In addition to photons from π^0 decays, the FMS measures electrons and positrons. It also has some sensitivity to charged hadrons, such as π^\pm . On average, a charged pion deposits about 1/3 of its energy in the FMS. If the π^0 is from the fragmentation of a high p_T jet, the FMS sees many of the associated hadronic fragments with degraded energy sensitivity. These charged hadron showers are fit to the photon shower shape and if the deposited energy is greater than 1 GeV, they are included in the list of low energy photon candidates. The FMS is triggered by high transverse momentum localized FMS signals. Because these cross sections have a severe transverse momentum dependence, the partially measured charged hadronic background contributes little to the trigger rate but does contribute background to π^0 photon pair signals at high p_T .

The events from the FMS were obtained from two trigger methods. The first method is called the board sum trigger, which demands transverse energy to be deposited in localized overlapping rectangles of the 32 FMS cells. The second method is called the jet trigger, which is satisfied by deposition of transverse energy, with a higher threshold than that of the board sum triggers, measured within overlapping azimuthal regions of angle $\Delta\phi = \pi/2$.

Three parallel implementations of the board sum triggers are used to select events, each with π^0 p_T above one of three adjustable thresholds, typically 1.6, 1.9 and 2.2 GeV/c. Triggers were prescaled to conserve detector readout bandwidth while sampling the different p_T regions with similar statistical uncertainties. The pp data sample presented in this paper corresponds to an integrated luminosity of 34 pb^{-1} using the highest threshold triggers, which are not prescaled. The corresponding analyzed luminosity for proton-nucleus collisions is $905 \text{ nb}^{-1} = \frac{24.5 \text{ pb}^{-1}}{27}$ and $206 \text{ nb}^{-1} = \frac{40.6 \text{ pb}^{-1}}{197}$ for $p\text{Al}$ and $p\text{Au}$, respectively, where the numerators are provided for direct comparison of proton-nucleon luminosities.

For each event, photon candidates are sorted into “cone clusters.” Each cone cluster includes a subset of the photon candidates for which the momentum direction is within an angular cone of 0.08 radians about the cone momentum direction of included photons. For each photon in the p_T sorted photon event list, the photon is tested for inclusion in the cone cluster list, testing the largest p_T clusters first. If not included in an existing cluster, this becomes the seed of a new cluster. Usually, only one of these cone clusters will be associated with the large p_T trigger. For this analysis of triggered events, only the leading p_T cone cluster is searched for π^0 candidates. This 0.08 radian cone radius, with nominal kinematic pair cuts and for the pion energies around 40 GeV, restricts the selected diphoton mass of photon pairs within a cone cluster to typically less than about 1 GeV/ c^2 . Searching for π^0 candidates within a cone cluster greatly reduces the combinatorial photon pair possibilities and reduces diphoton background.

At higher energy, the separation between π^0 photons becomes small, on the scale of the cell size. In this case, fits to a two photon hypothesis tend to overestimate the separation between these photons. For large energy pions, or equivalently large x_F , as seen in Fig. 2, calculated masses are preferentially smeared to larger values. The π^0 mass resolution is broadened significantly to higher mass for π^0 energies $E_{\pi^0} > 35 \text{ GeV}$ in the large cells (lower pseudo-rapidity region) and for energies above $E_{\pi^0} > 50 \text{ GeV}$ in the small cells and higher pseudo-rapidity region of the FMS.

The leading energy pair of photons in the highest p_T cluster was analyzed, with selection based on the decay distribution of that two-photon pair. The condition $Z < 0.7$ is utilized, where $Z = \frac{|E_1 - E_2|}{E_1 + E_2}$ and E_1 and E_2 are the energies of the two photons. This selection was preferred over a less restrictive one because it decreases background under the π^0 mass peak. It is the accounting for background under the π^0 peak that represents the majority of the systematic uncertainty for the measurement of A_N .

While it is the intention to measure A_N for inclusive π^0 production, the selection of the highest-energy two photons for the π^0 candidates does sacrifice 10-15% of the pions, depending on kinematics. In proton-nucleus collisions ($p\text{Al}$ and $p\text{Au}$), we apply an additional selec-

tion criterion in order to remove a specific RHIC background which is seen in the “abort-gap” events, between buckets where the nuclear beam is not present. These events are referred to as single-beam events. For pA collisions, we require that the east BBC have a minimum signal (caused by the breakup of the nuclei). This removes about 5% of the lowest activity including most peripheral collisions from this analysis, but also removes nearly all of the single-beam background. The residual single-beam background contributes significantly to the systematic error only for a few of the high- x_F bins.

The residual single-beam background fraction in each kinematic bin is estimated from events seen in the abort-gap bunches. The ratio of asymmetry for the single-beam background to the π^0 asymmetry is to be defined as R_{NB} , so $A_{NB} = R_{NB}A_N$, where A_N is the π^0 asymmetry in the particular kinematic bin. Consistent with asymmetries observed in the small number of events in the abort gap, we conservatively assume that $R_{NB} = 0.5 \pm 0.5$.

VI. THE INCLUSIVE A_N MEASUREMENTS

In this paper A_N for forward π^0 production is measured for pp , pAl , and pAu collisions. The high transverse momentum forward π^0 is detected with the FMS calorimeter, detecting pions with pion pseudo-rapidity $2.7 < \eta < 3.8$. Candidate photon pairs passing the selection are independently analyzed within kinematic regions of p_T and x_F . In Fig. 2, the diphoton mass, $M_{\gamma\gamma}$, distributions are shown for two example kinematic regions, for pp , pAl and pAu collisions. The two-photon mass distributions are initially fitted to a quadratic background shape plus a Gaussian pion shape in the mass region below the η peak. The Gaussian only approximately represents the shape of the pion peak and that Gaussian shape is only used to determine a mass range above the pion peak. To finally determine the background fraction, the quadratic background shape is constrained to be zero at a mass of zero and is fit to the mass distribution in the limited mass region above the pion peak. Examples of these background fits are shown in Fig. 2. The pion signal is obtained by counting the events in the pion peak, $0.015 < M_{\gamma\gamma} < 0.255$ GeV/ c^2 , and subtracting the fitted background contribution in that region. The typical fraction f_B of background under the pion peak ranges from about 20% at very low x_F to a few percent when the pion energy is larger. We define $A_B = R_B A_N$ is the asymmetry of the background under the π^0 peak where R_B is the fraction of non-pion background and A_N is the π^0 asymmetry.

The value $R_B = 0.33 \pm 0.33$ was conservatively determined based on the asymmetry in the mass region ($0.3 < M_{\gamma\gamma} < 0.4$ GeV/ c^2) above the pion peak and below the η meson peak. This background asymmetry cannot be well measured with significance within a single kinematic bin, but is estimated based on an average over many kinematic bins. Uncertainty in this background

correction is the most important contribution to the systematic uncertainty in the π^0 measurement of A_N . A_N for a given bin in x_F and p_T is extracted from the fits to the uncorrected asymmetries, $a_0(\phi)$, which is determined in each ϕ bin from the number of pions (N^\uparrow and N^\downarrow) detected when the proton polarization is up $^\uparrow$ /down $^\downarrow$ (see Fig. 3). The uncorrected asymmetry is

$$a_0(\phi) = \frac{N^\uparrow(\phi) - N^\downarrow(\phi)}{N^\uparrow(\phi) + N^\downarrow(\phi)}. \quad (5)$$

The azimuthal dependence of $a_0(\phi)$ is fit to the form

$$a_0(\phi) = p_0 + p_1 \cos \phi. \quad (6)$$

The parameter p_1 is proportional to A_N but must be corrected for the polarization of the proton beam P_B and a factor K to account for background effects,

$$A_N = p_1 \frac{K}{P_B}. \quad (7)$$

The beam polarization varied for different RHIC fills. The polarization and beam luminosity were largest at the start of a fill and decayed during the fill. To maximize the use of available data acquisition bandwidth, STAR adjusts the FMS trigger prescale factors during the fill, collecting a larger fraction of available low p_T cross section when the luminosity is lower. The analysis of RHIC polarization has been described by the RHIC Polarimetry group [35]. In this analysis, the average polarization for each kinematic data point is calculated by folding the run by run polarization with the trigger rate contributing to each kinematic point. For a given beam fill, there is variation in the average polarization of 1-2% for different kinematic regions. The variation of A_N from these different polarizations is small with respect to the overall uncertainties. The uncertainty on polarization is divided between scale uncertainties common throughout the running period and non-scale uncertainties that vary fill by fill. The scale uncertainties, $\Delta P/P$, are 3%, 3.1%, and 3.2% for pp , pAu , and pAl , respectively, and are not included in the point-by-point polarization measurement. When ratios of asymmetries are taken, the dominant polarization uncertainty, like many of the other systematic uncertainties, tends to cancel in the ratio.

In Eq. 7, K represents a correction factor to the asymmetry based on the estimates of backgrounds in the mass region $0.015 < M_{\gamma\gamma} < 0.255$ GeV/ c^2 . The largest part of the correction K of Eq. 7 was obtained from the background fraction f_B under the peak with asymmetry $A_B = R_B A_N$. The fraction f_{NB} represents a small additional background fraction (typically 1 to 3%) from interactions that cannot be associated with polarized pp or pA collisions with asymmetry $A_{NB} = R_{NB} A_N$. Then the factor K is

$$K = \left[\frac{1}{1 + f_B(R_B - 1)} \right] \left[\frac{1}{1 + f_{NB}(R_{NB} - 1)} \right]. \quad (8)$$

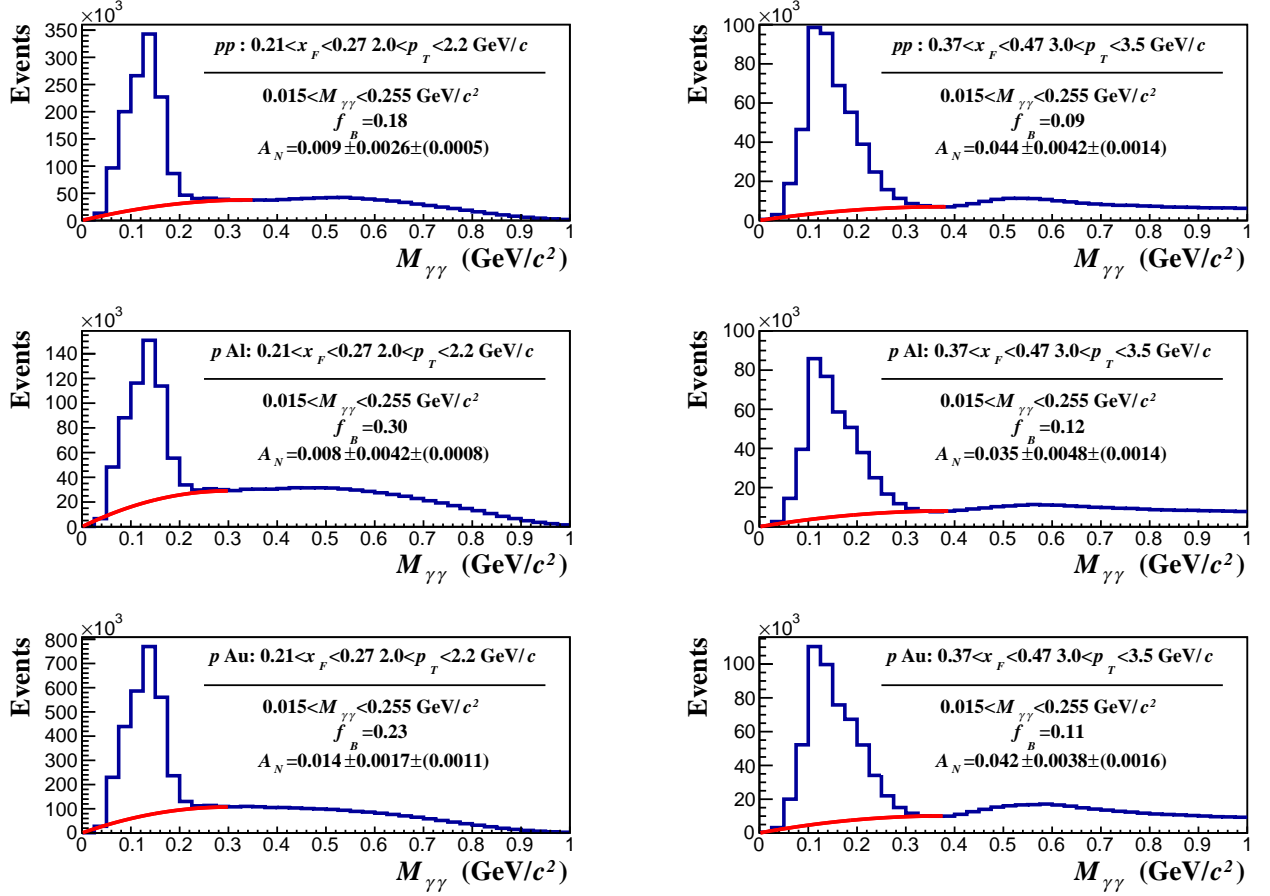


FIG. 2. Example invariant mass spectra for diphoton pairs selected within two kinematic regions (two columns) and three collision types (rows: pp , $p\text{Al}$, $p\text{Au}$). The asymmetries A_N for pion peaks are obtained within the mass region $0.015 < M_{\gamma\gamma} < 0.255 \text{ GeV}/c^2$. For the indicated fitted backgrounds under the peaks, the fraction of background events is f_B . The measured A_N for the π^0 , with all corrections applied, is included within each panel with statistical uncertainty followed by systematic uncertainty in parentheses.

The systematic uncertainties on A_N come from three sources: polarization error (typically $< 0.5\%$, excluding the overall polarization scale uncertainty); the beam background (typically $1 - 30\%$); and the single-beam background (typically $1 - 3\%$). The uncertainty in the multiplicative factor K is the largest source of systematic error in our measurement of A_N . These uncertainties are calculated individually for each given kinematic bin.

The various systematic contributions to our p_T uncertainty have been discussed in detail in a previous analysis [32]. The transverse momentum error analysis using that data, collected in 2012 and 2013, is applicable for these 2015 data. That analysis determined the final σ_{p_T}/p_T to be approximately 5-6%, an estimate we will adopt here. In both analyses, the dominant contribution lies in the uncertainty on the energy calibration of the detector ($\sigma_C \approx 5\%$). The energy calibration of the FMS is based on an analysis of the π^0 mass for 20-30 GeV π^0 photon pairs in the large cells and 40-50 GeV pairs in the small cells. We have conservatively set our final error in transverse momentum, $\sigma_{p_T}/p_T = 7\%$, allowing for minor

differences with this analysis and the previous analysis.

The value of the parameter p_0 from Eq. 6 indicates the asymmetry of relative integrated luminosity, as measured in the given kinematic region. RHIC spin patterns are changed for each fill so the integrated luminosities for spin up and spin down bunches are nearly equal. The distributions of parameters p_0 for the three collision system data sets (pp , $p\text{Al}$ and $p\text{Au}$) have weighted means of $(0.0032 \pm 0.0002, -0.0009 \pm 0.0002 \text{ and } 0.0001 \pm 0.0002)$, respectively. The fits over all kinematic regions to a single constant value, p_0 , have corresponding χ^2 values of 32, 57 and 45 for 40 kinematic regions (39 degrees of freedom). While the extracted values for A_N depend only on the p_1 parameter, it is seen from the above that the values of p_0 parameters are small and for each beam data set, the measurements of p_0 in different kinematic regions are internally consistent within each set.

An A_N point is extracted from each of 110 kinematic and “collisions beam type” bins based on the value of parameter p_1 from the fit to Eq. 6. As shown for a few example kinematic regions and beam types in Fig. 3,

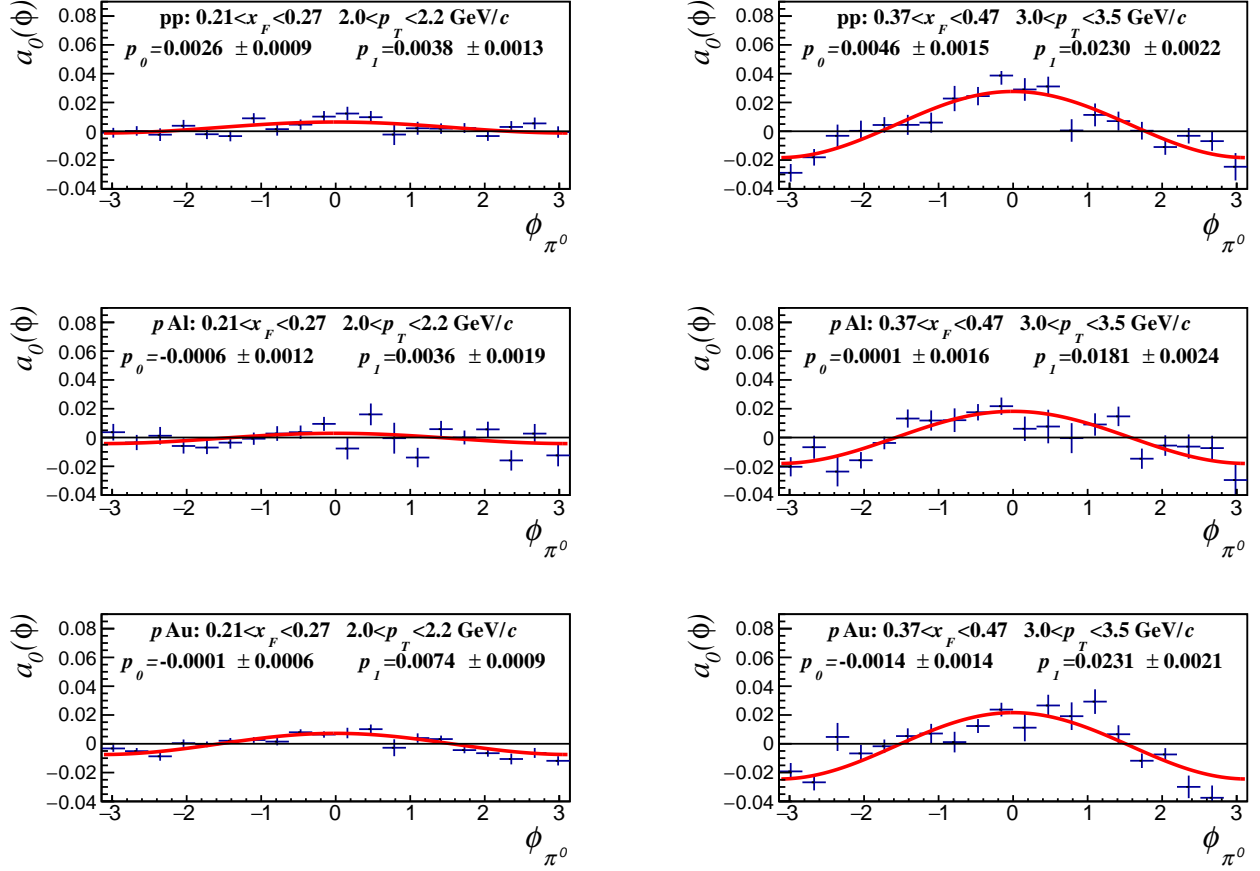


FIG. 3. Uncorrected transverse spin asymmetries for the same 6 kinematic regions as in Fig. 2. The azimuthal ϕ_{π^0} distributions of the uncorrected asymmetries, $a_0(\phi)$, are shown for events in the mass range $0.015 < M_{\gamma\gamma} < 0.255$ GeV/ c^2 . Fits to the functional form from Eq. 6 are shown with fitted parameter values p_0 and p_1 .

each two-parameter fit to the 20 azimuthal points results in a χ^2 value. Over this large ensemble of such fits, the distribution of measured χ^2 values is in good agreement with the theoretical χ^2 distribution. For the pp , pAl and pAu data sets, the average χ^2 s for the fits to Eq. 6 are 18.5, 18.1 and 18.4 for 18 degrees of freedom, respectively. The examples shown in Figs. 2 and 3 represent only six kinematic regions of 110 kinematic points at which A_N has been calculated. The transverse single-spin asymmetry for the full data set is shown in Fig. 4.

For each x_F region, the ratios of A_N for $pAu(pAl)$ to A_N for pp scattering are shown as a function of p_T in Fig. 5(6). The p_T dependences of these ratios are consistent with a constant ratio. Nevertheless, the A_N ratios shown in Fig. 5 and Fig. 6 were separately averaged for low p_T (1.5 GeV/ $c < p_T < 2.5$ GeV/ c) and high p_T ($p_T > 2.5$ GeV/ c). The fitted average values of A_N ratios for each plot in Figs. 5 and 6, averaging over the full p_T range for each x_F , are plotted in Fig. 7 as a function of $\log A$. The systematic uncertainties in Fig. 5 and Fig. 6 are reduced to account for the correlated background corrections between pp and pA distributions. The non-beam

backgrounds thus contribute the most to these systematic errors with statistical uncertainty dominating.

We parameterize the dependence of A_N on nuclear size A with a power law form

$$A_N(pA) = A_N(pp)A^P. \quad (9)$$

To determine the exponent P for each of the six x_F bins, the weighted means shown in Fig. 7 are fitted to the power law form,

$$r(pA) = \left\langle \frac{A_N(pA)}{A_N(pp)} \right\rangle_{all p_T} = A^P. \quad (10)$$

The ratios, $r(pA)$, as defined in Eq. 10, represent the ratio of nuclear suppression of A_N in pA to A_N observed pp scattering, averaged over the full observed p_T range. For each region of x_F , we fit to a power law in nuclear size A with a fitted exponent, P . Recognizing that the uncertainties in the ratio of pA to pp are correlated, the simple χ^2 fit in the figure can be biased in the determination of the exponent, P . We refer to this simple fit, with correlated uncertainties in the ratios, as a “Type 1” determination of P .

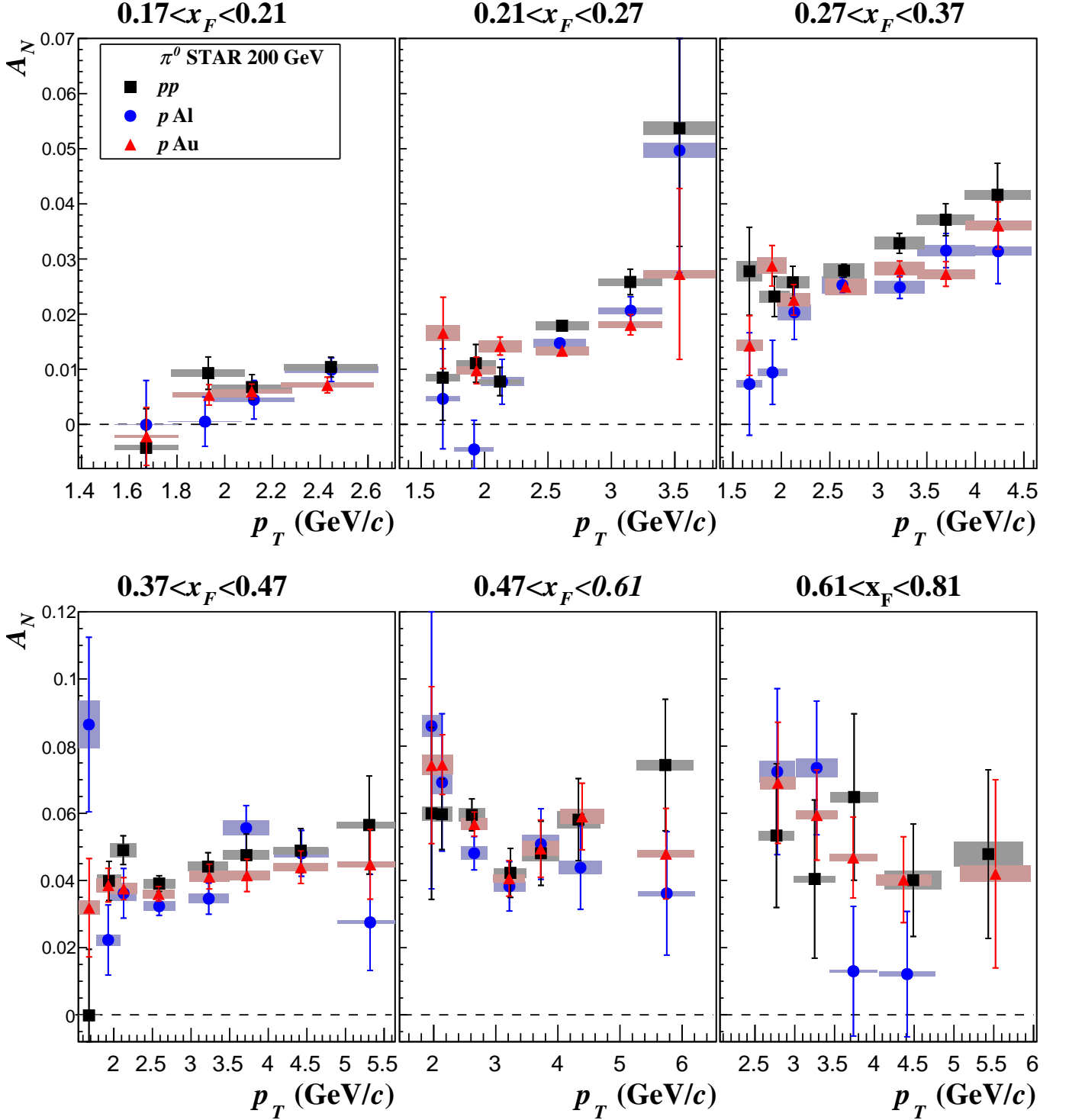


FIG. 4. The transverse momentum p_T dependence of A_N for 6 bins in Feynman x_F . The events contributing are inclusive π^0 s with selection in the invariant mass window $0.015 < M_{\gamma\gamma} < 0.255$ GeV/c². Results for the three collision systems are shown, black squares for pp , blue circles for $p\text{Al}$ and red triangles for $p\text{Au}$ collisions. The event selection criteria are given in the text. The statistical uncertainties are shown with vertical error bars and the filled boxes indicate the horizontal and vertical systematic uncertainties.

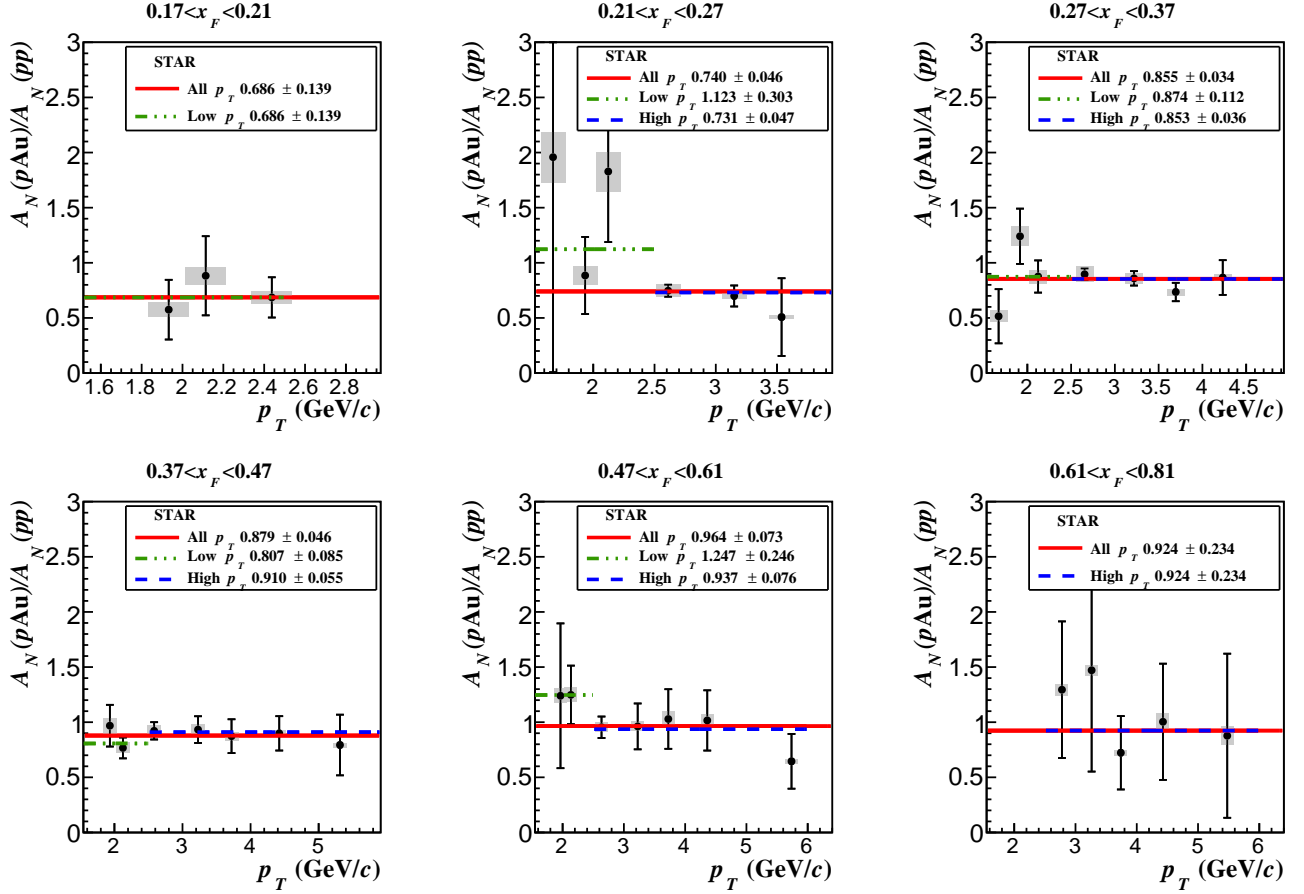


FIG. 5. The transverse momentum p_T dependence of the ratio of A_N for pAu scattering to that for pp for six Feynman x_F ranges. This figure refers to the same data as is plotted in Fig. 4. The event selection criteria are given in the text. The statistical uncertainties are shown with vertical error bars, and the filled boxes indicate systematic uncertainties appropriate for the ratio. Horizontal lines indicate the fit to the average ratio over the region $1.5 < p_T < 2.5$ GeV/c, $2.5 < p_T < 7.5$ GeV/c and for the combined p_T range.

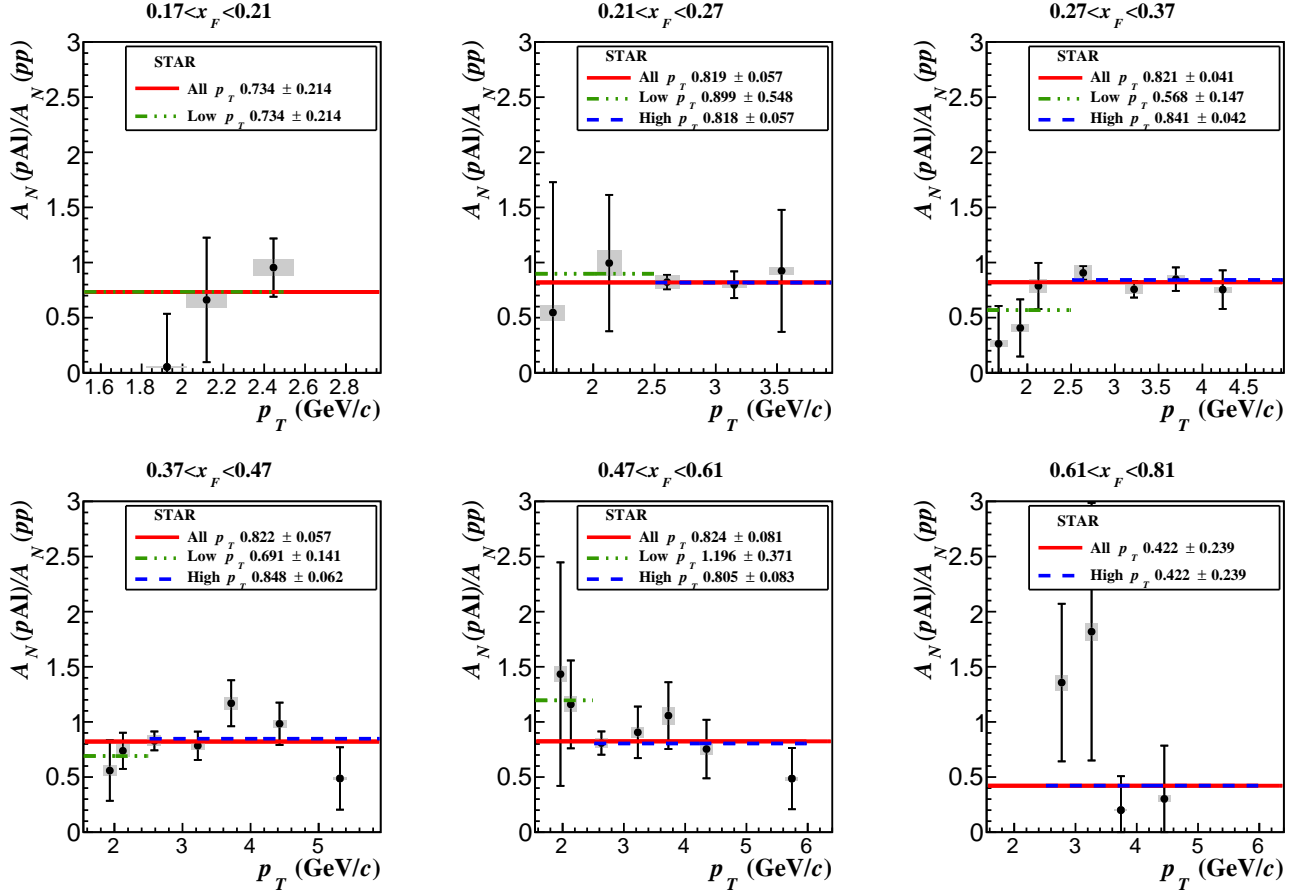


FIG. 6. Similar to Fig. 5 but the ratio of A_N in pAl to that in pp.

A second method for determining the exponent, P , without correlated uncertainties is to fit each point in p_T and x_F to the two-parameter form of Eq. 9, with parameters $A_N(pp)$ and P . These fits are two-parameter fits to three measurements within each kinematic region. Then with a weighted mean over p_T of the exponents from fits, an average P is obtained for each x_F region. This is referred to as the “Type 2” method, and the bands corresponding to the one sigma uncertainties in this “Type 2” fit are shown in Fig. 7 as the shaded regions.

The data points from all beams and all transverse momenta are combined in each of the six x_F bins shown in other figures, with centers located at $x_F = \{0.19, 0.24, 0.32, 0.42, 0.54, 0.71\}$. In Fig. 8, all data from pp, pAl and pAu collisions are combined and show the x_F dependence for several p_T regions. For $x_F < 0.47$, A_N seems to depend only weakly on transverse momentum, with a gentle increase in asymmetry at larger p_T , but at larger $x_F > 0.47$, it appears that A_N may flatten or perhaps falls with p_T .

Fitting the exponent of the A dependence of the ratios separately for the low and high p_T regions, the exponents

P_L and P_H are obtained,

$$r_L(pA) = \left\langle \frac{A_N(pA)}{A_N(pp)} \right\rangle_{p_T < 2.5 \text{ GeV/c}} = A^{P_L} \quad (11)$$

$$r_H(pA) = \left\langle \frac{A_N(pA)}{A_N(pp)} \right\rangle_{p_T > 2.5 \text{ GeV/c}} = A^{P_H}. \quad (12)$$

Calculations of A_N ratios by Hatta et al. [36] identify an amplitude that is thought to be dominant in the saturation region and would scale as $A_N \propto A^{-\frac{1}{3}}$ in $p^\uparrow + A \rightarrow \pi^0 X$. These calculations could apply to our present measurements of A_N for pp, pAl and pAu in the transverse momentum range $1.5 < p_T < 2.5$ GeV/c.

Comparing gold with $A=197$ and proton collisions with $A=1$, this implies a reduction of A_N for pAu by more than a factor of 5. Above the saturation region, they predict the A_N will scale as A^0 , indicating that the transverse single-spin asymmetry at larger p_T could be similar for pp and pAu collisions. The fitted values of the exponents P_L and P_H as functions of x_F are shown in Fig. 9. The exponents are generally within about 5% of zero in both the low and high p_T regions and significantly different from the value of $-\frac{1}{3}$ that has been predicted to apply in the region below the saturation scale.

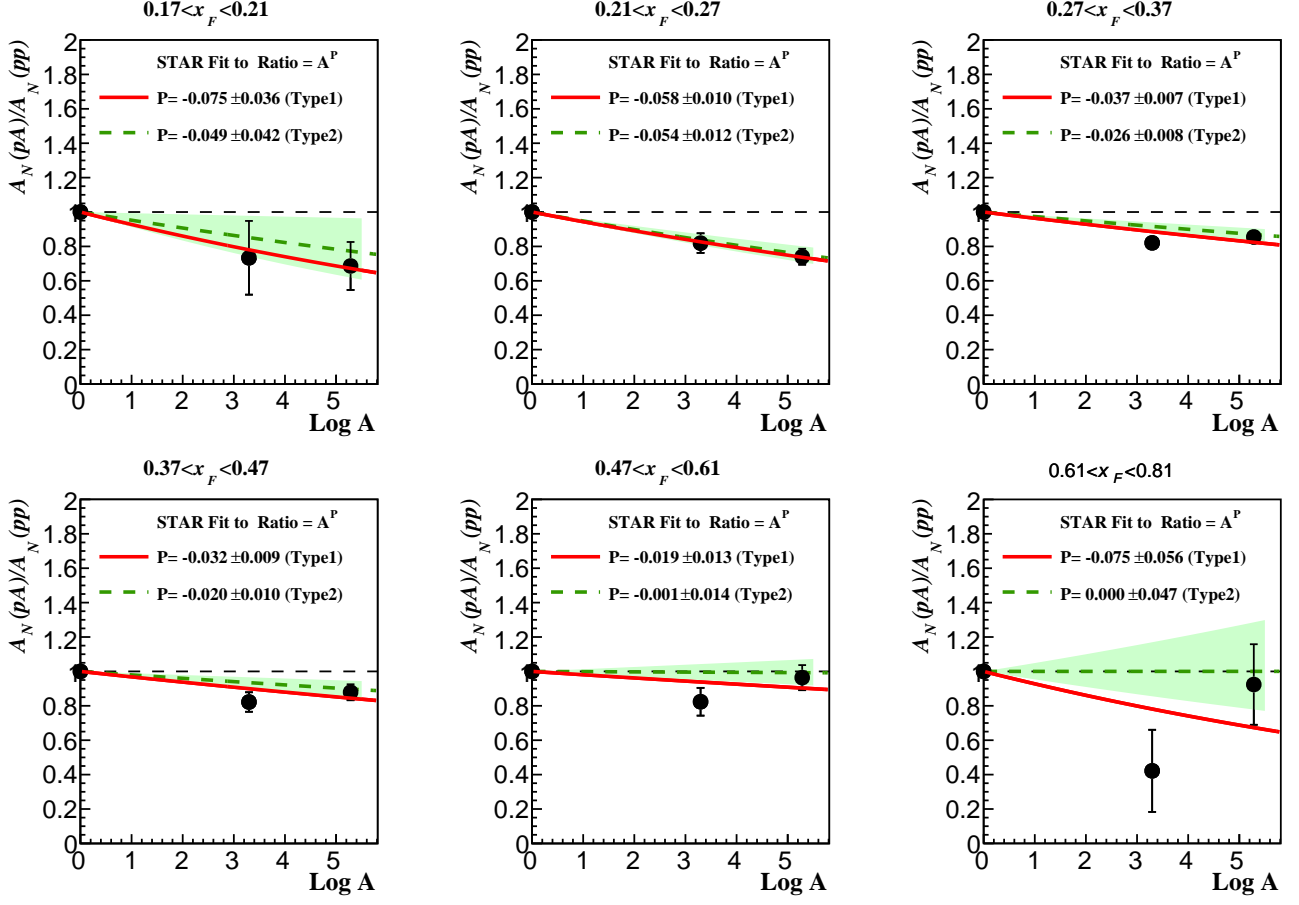


FIG. 7. The ratio of A_N for pA scattering to that for pp scattering is shown for six x_F regions, averaging over the full range of p_T dependence. The fitted form for these ratios as a function of A is obtained using Type 1 and Type 2 analyses as described in the text. The dependence of A_N as a function of $\log A$ is displayed with a filled error band, obtained from the Type 2 analysis, shown as the dashed line.

Another approach [37], based on a geometrical scaling of gluon distributions and with Collins-type fragmentation, has also been used to calculate the transverse single-spin asymmetry. They predicted that for pion transverse momentum below the saturation scale, $p_T^2 \ll Q_s^2$, the A_N ratio is $A_N(pA)/A_N(pp) \simeq \frac{Q_{sp}^2}{Q_{sA}^2}$, where Q_{sA}^2 is the square of the saturation scale for a nucleus with A nucleons. For p_T well above the saturation scale, the ratio was expected to be 1. Models, which suggest that at large p_T the ratio should approach a form with exponent zero, are in good agreement with these data.

VII. ISOLATED A_N MEASUREMENTS

It is observed here that the presence of soft photons or hadronic fragments in the vicinity of the highest p_T pion can decrease the asymmetry significantly, cutting A_N in half in most kinematic regions. For a subset of the events shown in Fig. 4, there are exactly two photons with en-

ergy greater than 1 GeV in the 0.08 radian cone around the π^0 event. We refer to “isolated” events as those with a highest p_T cone cluster with only a single pair of photon candidates. “Non-isolated” events are more jet-like, having at least three photon candidates within the cone. For a large fraction of the covered kinematics, about 1/3 of the inclusively selected π^0 events contributing to Fig. 4 have an isolated π^0 . These more exclusive events have generally larger values of A_N .

It is seen from the comparison of Fig. 4 with Figs. 10, 11, and 12 that A_N for isolated π^0 s is significantly greater than for the complementary part of the inclusive event set with additional fragments observed.

The electromagnetic calorimeter has limited sensitivity to charged pions, so isolation does not guarantee the absence of hadrons other than π^0 s. However, this observation hints at the possibility that the asymmetry for jets with a leading energy π^0 is much less than the single π^0 asymmetry in this forward kinematic region. The enhanced A_N for events with no observed jet fragment may indicate that these events are not related to jet pro-

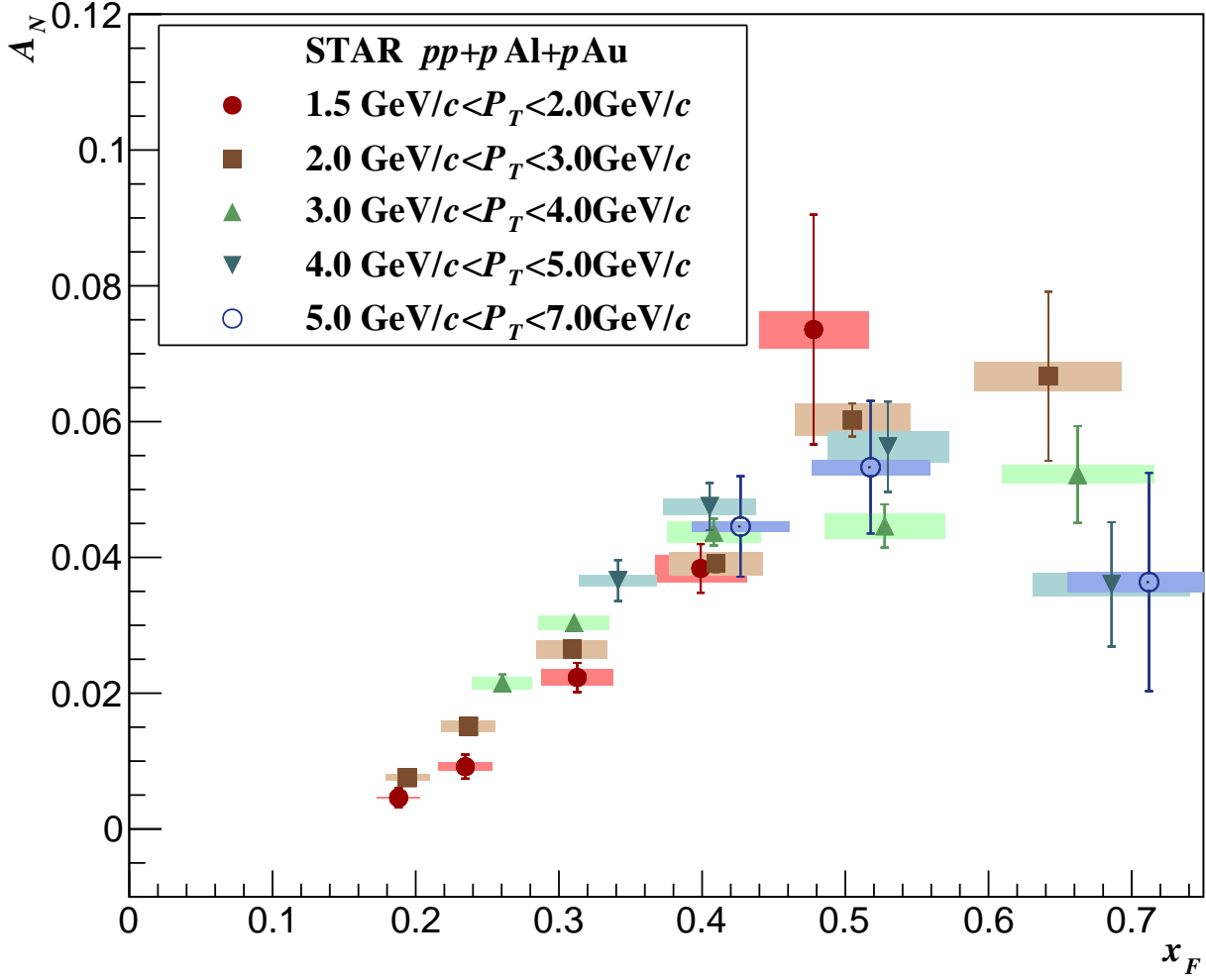


FIG. 8. The x_F dependence of the π^0 A_N is shown with data from the combined pp , $p\text{Al}$, and $p\text{Au}$ data points, collecting points within x_F intervals for frames from Fig.4 and the indicated p_T range. Data points are shown separately for five intervals of transverse momentum indicated by different symbols and plotted horizontally at the average x_F for each combined point. Vertical error bars represent statistical uncertainties and the systematic horizontal and vertical uncertainties are shown with filled boxes.

duction with fragmentation.

The observation that isolated π^0 events have larger A_N does not appear to depend upon the nuclear size A in pA collisions. In Fig. 13 the determination of the exponent P in the A dependence, defined in Eq. 9, has been analyzed separately for isolated and non-isolated events. The average exponents are similar for these two subsets of the data.

This dependence of the measured A_N on event topology is further described in a jet analysis [39], with some of these same data. Although technical aspects of that analyses differ from this one, the results are consistent in those cases where the same quantity is measured.

VIII. CONCLUSIONS

This new measurement of A_N for forward π^0 production, in pp , $p\text{Al}$ and $p\text{Au}$ collisions, determines the dependence on x_F and p_T . It is observed that A_N generally increases with increasing p_T at fixed x_F ($0.17 < x_F < 0.47$), for p_T up to 5 GeV/c. In many calculations, exemplified by the simple model of Eq. 4, A_N is expected to fall with p_T when p_T is significantly larger than some nominal QCD scale k_T , representing the spin dependent part of the transverse momentum shift due to initial or final interactions. The persistent rise in A_N for p_T well beyond the 1 GeV/c scale, is unexpected.

Furthermore, the asymmetry A_N , for forward π^0 pro-

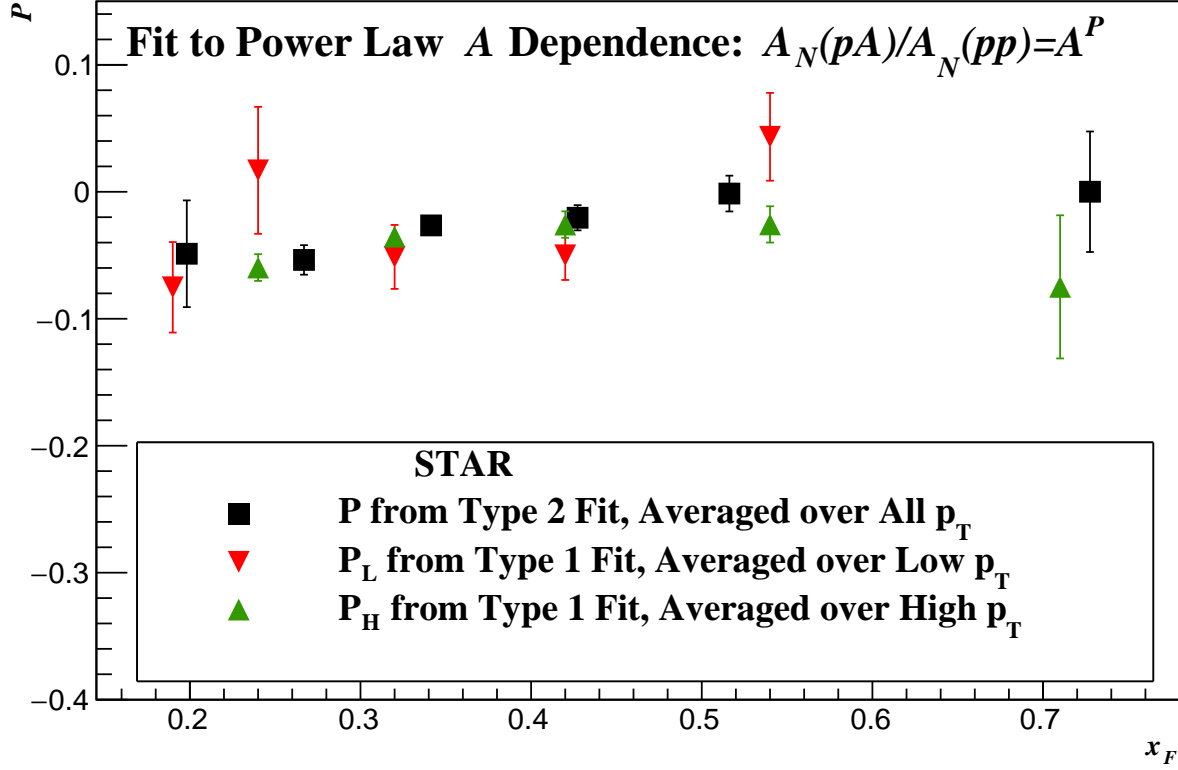


FIG. 9. Analyzing separately the low p_T ($1.5 < p_T < 2.5$ GeV/c) data and the higher p_T data, the exponent, P , for nuclear A dependence of the asymmetry ratio $\frac{A_N(pA)}{A_N(pp)} = A^P$ is shown as a function of x_F . Points are included, averaging over the low p_T region and high p_T regions ($p_T > 2.5$ GeV/c) separately. Examples of one parameter power law fits for P are shown in Fig. 7, where power dependence exponent P is plotted as a function of Feynman x_F . The uncertainties shown are from fits described in the text and are dominated by statistical uncertainties. The systematic uncertainties are small, mostly cancelling, in ratios between different nuclear A data sets and are not separately shown.

duction is significantly larger for events with an observed isolated π^0 than for events that show evidence of additional fragmentation products. It is interesting to compare this result to the published A_N for jets, from [19], where the asymmetry was observed to be small compared to this π^0 measurement. The Siverts picture, where a proton spin dependent transverse momentum k_T is acquired from initial state interactions, is not the natural choice for explaining the difference in A_N for isolated and non-isolated π^0 s in the final state. But neither is the enhancement of A_N for isolated pions expected in the Collins picture, where jet fragmentation into multiple hadrons imparts a spin dependent momentum k_T to the observed pion, to generate pion asymmetry.

The kinematic dependence of A_N on x_F and p_T is similar for the three collision systems. The suppression of A_N in collisions with nuclear beams is modest, with the typical A_N ratios between pA and pp greater than 80%. When the suppression of A_N is fit to a power law nu-

clear A dependence, $A_N(A) \propto A^P$, the measured exponents are in the range of $0.0 < P < 0.075$. The weighted average exponent from Type 2 fits in Fig. 9 is $\langle P \rangle = -0.027 \pm 0.005$. This corresponds to a reduction of $r(\text{Au}) = 0.87 \pm 0.02$. For the Type 1 fits in the low p_T region, the weighted average is $\langle P_L \rangle = -0.037 \pm 0.013$, implying $r_L(\text{Au}) \simeq 0.82 \pm 0.06$. In the high p_T region, the weighted average is $\langle P_H \rangle = -0.039 \pm 0.0048$, implying $r_H(\text{Au}) \simeq 0.81 \pm 0.02$.

This nuclear suppression of π^0 A_N is much less than that reported by the PHENIX collaboration, for positively charged hadrons at somewhat lower pseudorapidity. The fits from the PHENIX measurement favored an exponent $P = -0.37$ [38], with a quoted statistical uncertainty range ($-0.60 < P < -0.27$). Unlike the result of this paper, the PHENIX results are nominally consistent with the prediction of Hatta et al., ($P = -1/3$).

It is noted that the range of x_F coverage by the

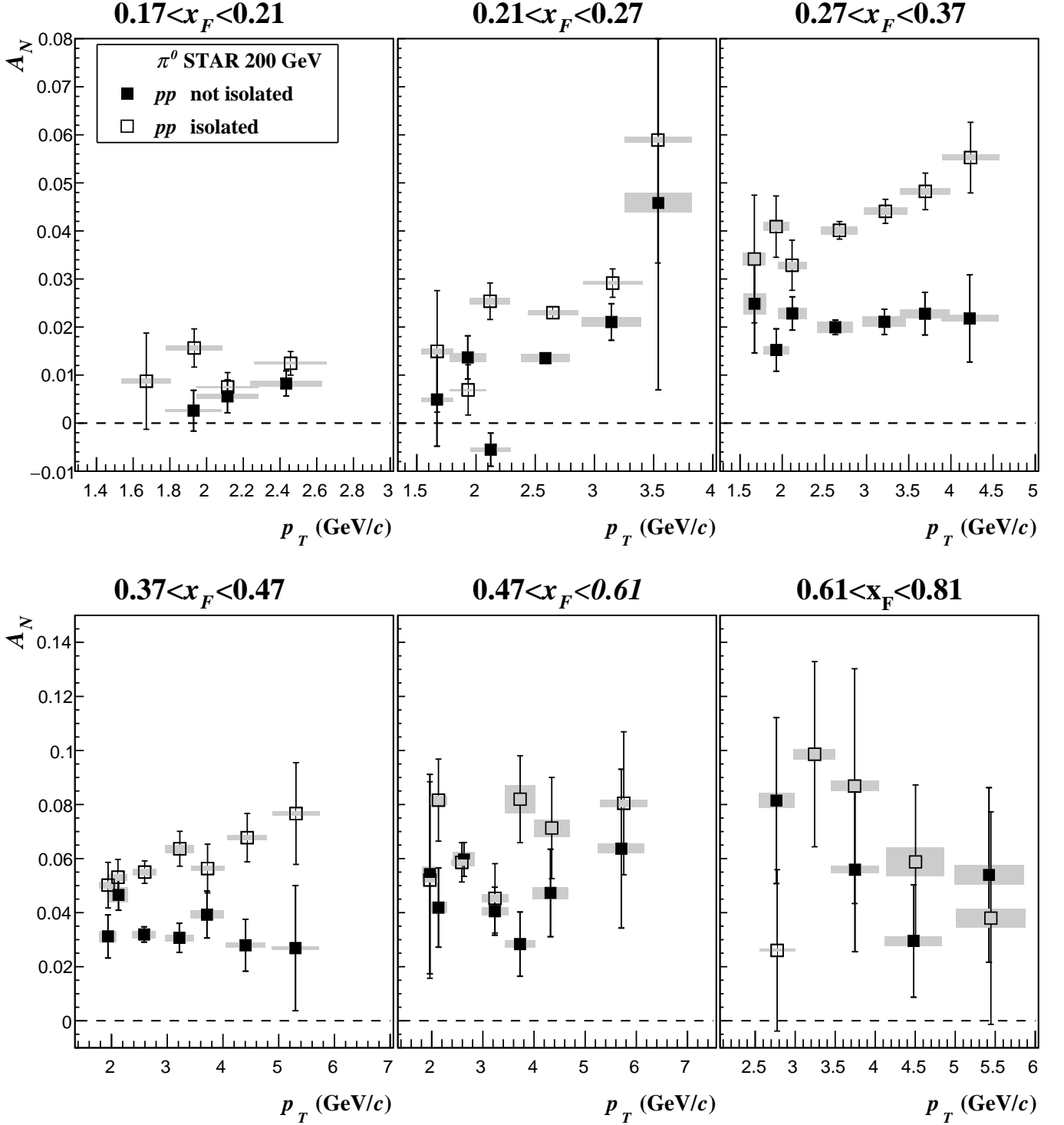


FIG. 10. The transverse momentum p_T dependence of A_N for pion production in six (x_F) regions for pp collisions. The data from Fig. 4 have been divided into two parts based on whether the π^0 is produced with additional jet-like fragments of energy more than 1 GeV, shown with filled markers, or in isolation shown with open markers. The event selection criteria for isolated and non-isolated events are given in the text. The statistical uncertainties are shown with vertical error bars. The filled boxes indicate horizontal and vertical systematic uncertainties.

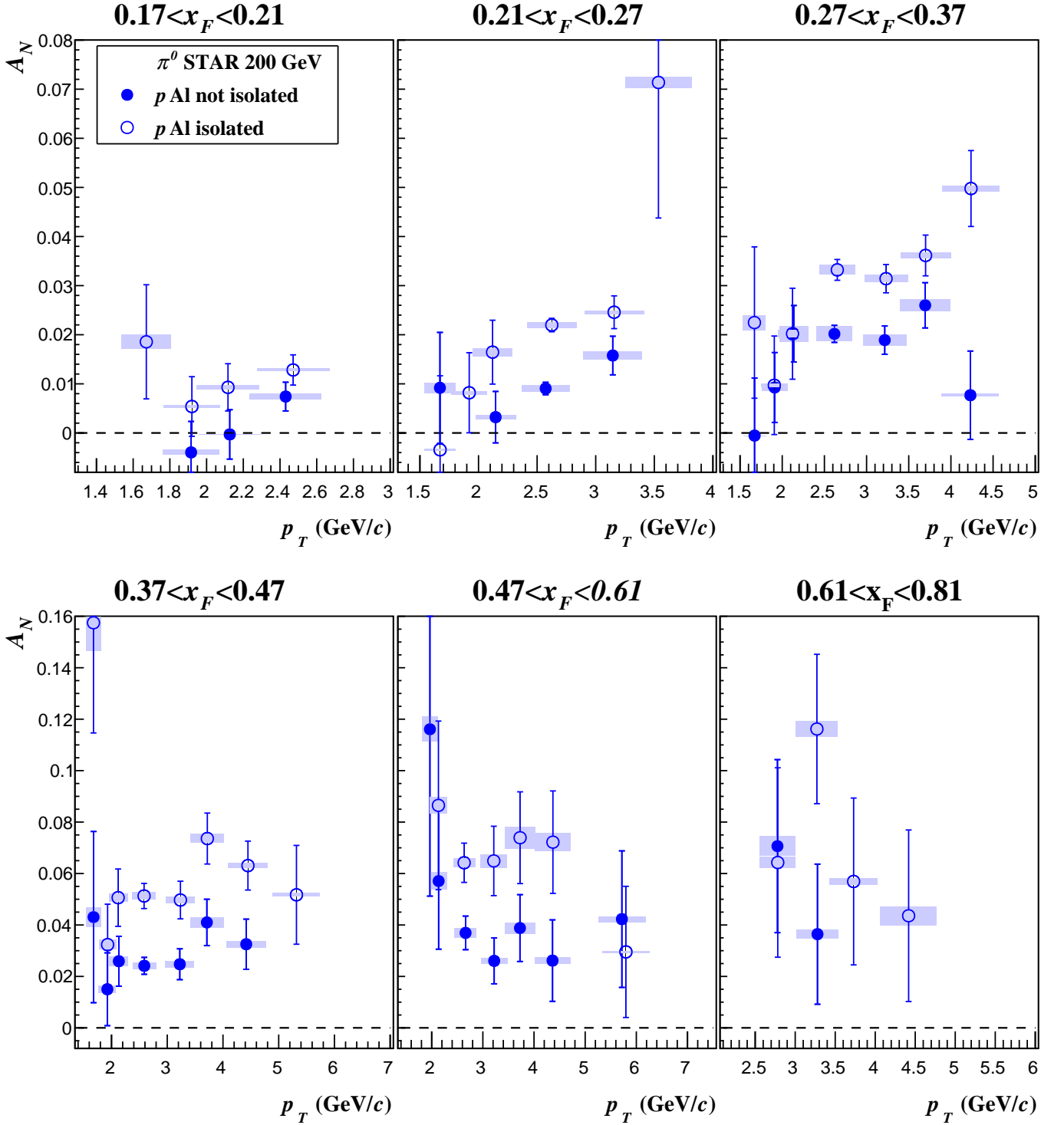


FIG. 11. This plot is similar to Fig. 10 but for pAl collisions.

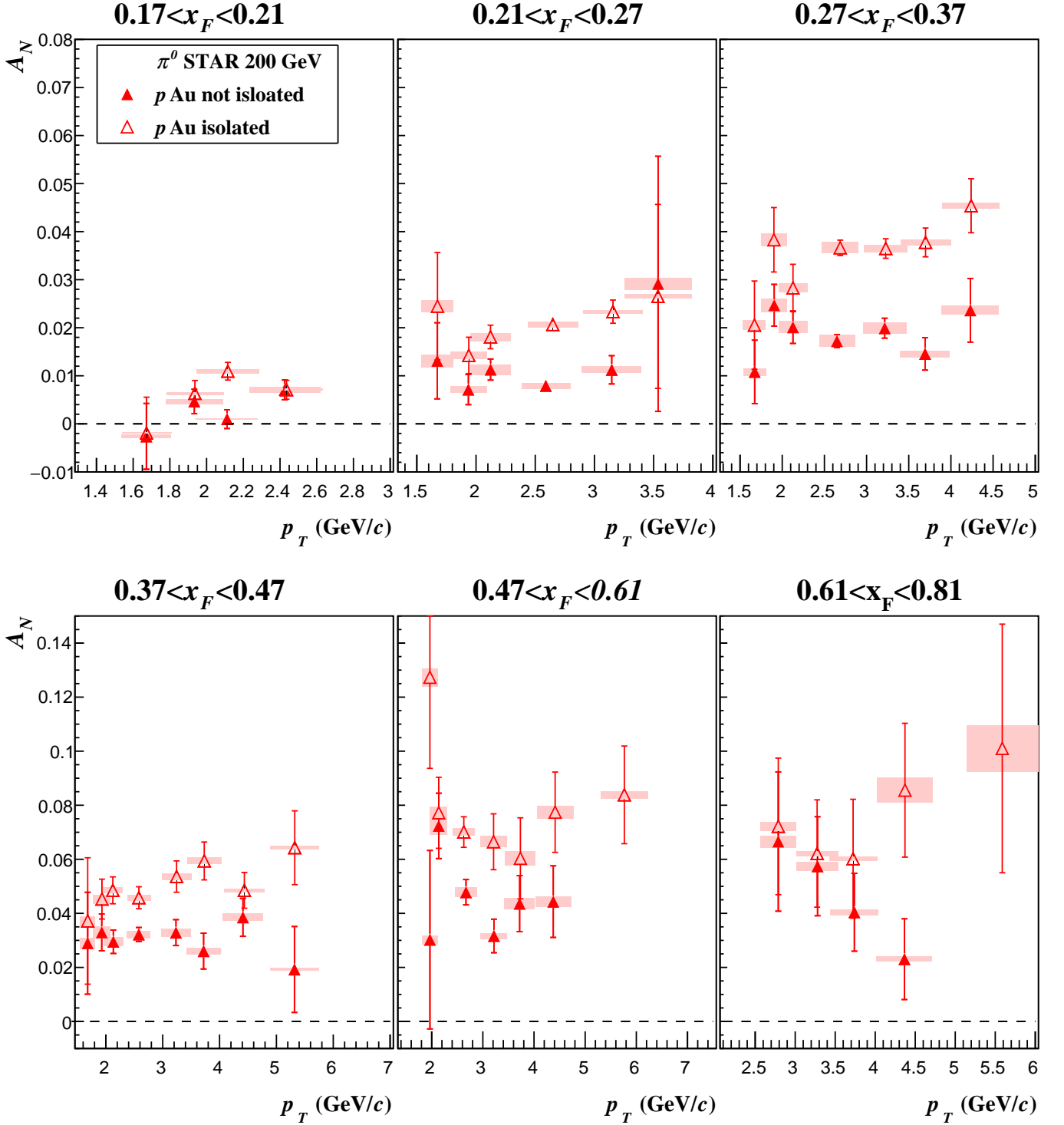


FIG. 12. This plot is similar to Fig. 10 but for p Au collisions.

PHENIX measurement, $0.1 < x_F < 0.2$, is below the range presented here, shown in Fig. 9. The range of gluon momentum fractions, x , probed within the nuclear beams in this measurement is $x < 0.004$. This is below the range probed in the PHENIX measurement, $x > 0.004$. It is

also noted, from the distribution of exponents shown in Fig. 9, that the P exponents are seen to slowly increase with x_F , with an average slope $dP/dx_F = 0.16 \pm 0.06$ for the Type 2 fits. But there is no significant difference between the exponent P_H in the higher p_T region and

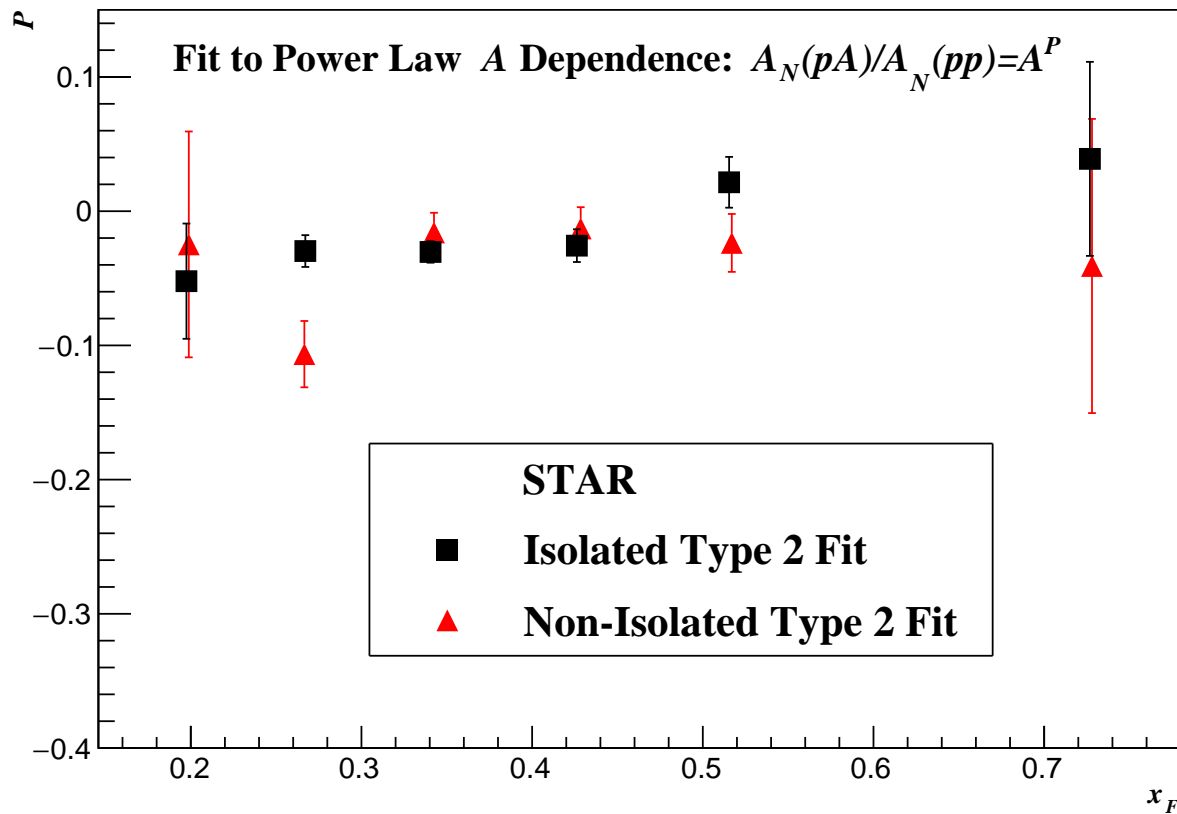


FIG. 13. Comparison of the nuclear A dependence of A_N for events with isolated π^0 s and events with non-isolated π^0 s. The exponent P of the nuclear A dependence is shown as a function of x_F . The exponent is defined in Eq. 9. The points shown are averaged over the full p_T range with a Type 2 fit at each p_T and x_F similar to the points of Fig. 9.

P_L in the low p_T region, where gluon saturation effects could be most relevant. The general agreement between Type 1 and Type 2 fits helps to give confidence in the fitting methods.

Combining all beam types to maximize statistics for A_N measurements, for Feynman $x_F < 0.47$ the asymmetry A_N increases with x_F and with p_T . For $x_F > 0.47$ the trend moderates, as the dependence of A_N on p_T flattens or may begin to fall with p_T over the measured p_T range.

These measurements of the dependence of A_N , for forward π^0 production, on kinematics and event topology, should provide new input for ongoing theoretical studies of the underlying dynamics for these processes. In pA collisions, the dependence of A_N on nuclear size A has been measured and is small.

ACKNOWLEDGMENTS

We thank the RHIC Operations Group and RCF at BNL, the NERSC Center at LBNL, and the Open Sci-

ence Grid consortium for providing resources and support. This work was supported in part by the Office of Nuclear Physics within the U.S. DOE Office of Science, the U.S. National Science Foundation, the Ministry of Education and Science of the Russian Federation, National Natural Science Foundation of China, Chinese Academy of Science, the Ministry of Science and Technology of China and the Chinese Ministry of Education, the Higher Education Sprout Project by Ministry of Education at NCKU, the National Research Foundation of Korea, Czech Science Foundation and Ministry of Education, Youth and Sports of the Czech Republic, Hungarian National Research, Development and Innovation Office, New National Excellency Programme of the Hungarian Ministry of Human Capacities, Department of Atomic Energy and Department of Science and Technology of the Government of India, the National Science Centre of Poland, the Ministry of Science, Education and Sports of the Republic of Croatia, RosAtom of Russia and German Bundesministerium für Bildung, Wissenschaft, Forschung und Technologie (BMBF), Helmholtz Association, Ministry of Education, Culture, Sports, Science,

and Technology (MEXT) and Japan Society for the Promotion of Science (JSPS).

-
- [1] R. D. Klem, J. E. Bowers, H. W. Courant, H. Kagan, M. L. Marshak, E. A. Peterson, K. Ruddick, W. H. Dragoset, and J. B. Roberts, Measurement of Asymmetries of Inclusive Pion Production in Proton Proton Interactions at 6-GeV/c and 11.8-GeV/c. *Phys. Rev. Lett.* 36, 929 (1976).
- [2] S. Saroff et al, Single Spin Asymmetry in Inclusive Reactions Polarized P , P Goes to π^+ , π^- , and P at High $P(t)$ at 13.3-GeV/c and 18.5-GeV/c. *Phys. Rev. Lett.* 64, 995 (1990).
- [3] D. L. Adams et al, Comparison of spin asymmetries and cross-sections in π^0 production by 200-GeV polarized anti-protons and protons. *Phys. Lett.* B261, 201 (1991).
- [4] D.L. Adams et al, Analyzing power in inclusive π^+ and π^- production at high $x(F)$ with a 200-GeV polarized proton beam. *Phys. Lett.* B264, 462 (1991).
- [5] I. Arsene et al, Single Transverse Spin Asymmetries of Identified Charged Hadrons in Polarized p+p Collisions at $\sqrt{s} = 62.4$ -GeV. *Phys. Rev. Lett.* 101, 042001 (2008).
- [6] A. Adare et al, Measurement of transverse-single-spin asymmetries for midrapidity and forward-rapidity production of hadrons in polarized p+p collisions at $\sqrt{s} = 200$ and 62.4 GeV. *Phys. Rev.* D90, 012006 (2014).
- [7] B.I. Abelev et al, Forward Neutral Pion Transverse Single Spin Asymmetries in p+p Collisions at $\sqrt{s} = 200$ -GeV. *Phys. Rev. Lett.* 101, 222001 (2008).
- [8] J. D. Bjorken, Inelastic Scattering of Polarized Leptons from Polarized Nucleons. *Phys. Rev.* D1, 1376 (1970).
- [9] M. J. Alguard et al, Deep Inelastic Scattering of Polarized Electrons by Polarized Protons. *Phys. Rev. Lett.* 37, 1261 (1976).
- [10] J. Ashman et al, A Measurement of the Spin Asymmetry and Determination of the Structure Function $g(1)$ in Deep Inelastic Muon-Proton Scattering. *Phys. Lett.* B206, 364 (1988).
- [11] Daniel de Florian, Rodolfo Sassot, Marco Stratmann, and Werner Vogelsang, Extraction of Spin-Dependent Parton Densities and Their Uncertainties. *Phys. Rev.* D80, 034030 (2009).
- [12] Emanuele R. Nocera, Richard D. Ball, Stefano Forte, Giovanni Ridolfi, and Juan Rojo, A first unbiased global determination of polarized PDFs and their uncertainties. *Nucl. Phys.* B887, 276 (2014).
- [13] Daniel de Florian, Rodolfo Sassot, Marco Stratmann, and Werner Vogelsang, Evidence for polarization of gluons in the proton. *Phys. Rev. Lett.* 113, 012001 (2014).
- [14] Gordon L. Kane, J. Pumplin, and W. Repko, Transverse Quark Polarization in Large $p(T)$ Reactions, e^+e^- Jets, and Lepton Production: A Test of QCD. *Phys. Rev. Lett.* 41, 1689 (1978).
- [15] John C. Collins, Davison E. Soper, and George F. Sterman, Factorization of Hard Processes in QCD. *Adv. Ser. Dir. High Energy Phys.* 5, 1 (1989).
- [16] D. W. Sivers, Hard scattering scaling laws for single spin production asymmetries. *Phys. Rev.* D43, 261 (1991).
- [17] J. C. Collins, S. F. Heppelmann, and G. A. Ladinsky, Measuring transversity densities in singly polarized hadron hadron and lepton - hadron collisions. *Nucl. Phys.* B420, 565 (1994).
- [18] J. Qiu and G. Sterman, Single transverse-spin asymmetries in hadronic pion production. *Phys. Rev.* D59, 014004 (1999).
- [19] L. C. Bland et al, Cross Sections and Transverse Single-Spin Asymmetries in Forward Jet Production from Proton Collisions at $\sqrt{s} = 500$ GeV. *Phys. Lett.* B750, 660 (2015).
- [20] Stanley J. Brodsky, Dae Sung Hwang, and Ivan Schmidt, Initial-state interactions and single-spin asymmetries in Drell-Yan processes. *Nucl. Phys.* B642, 344 (2002).
- [21] John C. Collins, Leading twist single transverse-spin asymmetries: Drell-Yan and deep inelastic scattering. *Phys. Lett.* B536, 43 (2002).
- [22] C. Kouvaris, J. Qiu, W. Vogelsang, and F. Yuan, Single transverse-spin asymmetry in high transverse momentum pion production in p p collisions. *Phys. Rev.* D74, 114013 (2006).
- [23] M. Anselmino, M. Boglione, U. D'Alesio, S. Melis, F. Murgia, and A. Prokudin, Sivers effect and the single spin asymmetry A_N in $p^\uparrow p \rightarrow hX$ processes. *Phys. Rev.* D88, 054023 (2013).
- [24] Koichi Kanazawa, Yuji Koike, Andreas Metz, and Daniel Pitonyak, Towards an explanation of transverse single-spin asymmetries in proton-proton collisions: the role of fragmentation in collinear factorization. *Phys. Rev.* D89, 111501 (2014).
- [25] M. Anselmino, U. D'Alesio, and S. Melis, Transverse single-spin asymmetries in proton-proton collisions at the AFTER@LHC experiment in a TMD factorisation scheme. *Adv. High Energy Phys.* 2015, 475040 (2015).
- [26] Leonard Gamberg, Zhong-Bo Kang, Daniel Pitonyak, Marc Schlegel, and Shinsuke Yoshida, Polarized hyperon production in single-inclusive electron-positron annihilation at next-to-leading order. *JHEP* 01, 111 (2019).
- [27] Yuri V. Kovchegov and Matthew D. Sievert, A New Mechanism for Generating a Single Transverse Spin Asymmetry. *Phys. Rev.* D86, 034028 (2012).
- [28] Yuri V. Kovchegov and M. Gabriel Santiago, Lensing Mechanism Meets Small- x Physics: Single Transverse Spin Asymmetry in $p^\uparrow + p$ and $p^\uparrow + A$ Collisions. *Phys. Rev.* D102, 014022 (2020).
- [29] Edmond Iancu, Andrei Leonidov, and Larry D. McLerran, Nonlinear gluon evolution in the color glass condensate. 1. *Nucl. Phys.* A692, 583 (2001).
- [30] John Adams et al, Forward neutral pion production in p+p and d+au collisions at $\sqrt{s} = 200$ -GeV. *Phys. Rev. Lett.* 97, 152302 (2006).
- [31] I. Arsene et al, On the evolution of the nuclear modification factors with rapidity and centrality in d + Au collisions at $\sqrt{s} = 200$ -GeV. *Phys. Rev. Lett.* 93, 242303 (2004).
- [32] Jaroslav Adam et al, Longitudinal Double-Spin Asymmetries for π^0 s in the Forward Direction for 510 GeV Polarized pp Collisions. *Phys. Rev.* D98, 032013 (2018).
- [33] J. Kirelyuk, Local polarimetry for proton beams with the STAR beam beam counters. In *Spin physics. Polarized electron sources and polarimeters. Proceedings, 16th International Symposium, SPIN 2004, Trieste, Italy, October 10-16, 2004, and Workshop, PESP 2004, Mainz, Germany, October 7-9, 2004*, pages 718 (2005).

- [34] C. A. Whitten, The beam-beam counter: A local polarimeter at STAR. *AIP Conf. Proc.* 980, 390 (2008).
- [35] W. B. Schmidke, RHIC polarization for Runs 9-17. Technical Report BNL-209057-2018-TECH, Brookhaven National Laboratory (2018). <https://technotes.bnl.gov/Home/ViewTechNote/209057> (Unpublished).
- [36] Yoshitaka Hatta, Bo-Wen Xiao, Shinsuke Yoshida, and Feng Yuan, Single spin asymmetry in forward pA collisions II: Fragmentation contribution. *Phys. Rev. D* 95, 014008 (2017).
- [37] Zhong-Bo Kang and Feng Yuan, Single Spin Asymmetry Scaling in the Forward Rapidity Region at RHIC. *Phys. Rev. D* 84, 034019 (2011).
- [38] C. Aidala et al, Nuclear Dependence of the Transverse Single-Spin Asymmetry in the Production of Charged Hadrons at Forward Rapidity in Polarized $p + p$, $p+Al$, and $p+Au$ Collisions at $\sqrt{s_{NN}} = 200$ GeV. *Phys. Rev. Lett.* 123, 122001 (2019).
- [39] J. Adams et al, Measurement of transverse single-spin asymmetries of π^0 and electromagnetic jets at forward rapidity in 200 and 500 GeV transversely polarized proton-proton collisions. *To Be Published*.